AGRIVOLTAICS APPLICATION USING HOLOGRAPHIC OPTICAL ELEMENTS

by

Eli Salay

A MS Report Submitted to the Faculty of the

DEPARTMENT OF OPTICAL SCIENCES

In Partial Fulfillment of the Requirements

For the Degree of

MASTER OF SCIENCE

In the Graduate College

THE UNIVERSITY OF ARIZONA

2021

THE UNIVERSITY OF ARIZONA
GRADUATE COLLEGE

As members of the Master's Committee, we certify that we have read the MS report prepared by Elias John Salay, titled *Agrivoltaics Application Using Holographic Optical Elements* and recommend that it be accepted as fulfilling the dissertation requirement for the Master's Degree.

_____ Date: _____
Raymond Kostuk

_____ Date: _____
Pierre-Alexandre Blanche

_____ Date: _____
Kelly Potter

Final approval and acceptance of this MS report is contingent upon the candidate's submission of the final copies of the MS report to the Graduate College.

I hereby certify that I have read this MS report prepared under my direction and recommend that it be accepted as fulfilling the Master's requirement.

_____ Date: _____
Raymond Kostuk
Master's Report Committee Chair
Electrical and Computer Engineering & Optical Sciences

Acknowledgments

I would first like to thank my Master's Report advisor Dr. Raymond Kostuk of the College of Electrical and Computer Engineering and the College of Optical Sciences at the University of Arizona. I greatly appreciate the knowledge that he shared and the opportunity he provided to gain experience in his lab.

I would also like to thank my friends and family who supported me throughout my time at the University, especially my Mom and Dad who were there for me every step of this journey.

Table of Contents

List of Figures

List of Tables

Abstract

Agrivoltaics is a technology that has received increased attention in recent years as global warming has become an ever more pressing issue, as growing global populations continue to increase the demand for food and energy, and because farmland accounts for a significant portion of the world's terrestrial area. It is an innovative approach to meet the growing demand for both food and energy in which solar photovoltaics (solar panels) are added to agricultural regions to enable food-energy-water synergies. The colocation of photovoltaics and agricultural regions poses unique challenges that require unique solutions to optimize plant growth and energy production. For example, designs utilizing holographic optical elements or dichroic film to split the solar spectrum could be employed to improve the energy conversion efficiency of the photovoltaics and still support optimal plant growth.

This work examines a potential agrivoltaic design that considers combining cascaded holographic optical elements with two photovoltaic cells in order to support both plant growth and energy production. Cascaded holographic optical gratings lining the top of the structure diffract a portion of the solar spectrum to the solar panel while allowing the photosynthetically active radiation to transmit to the crop area. A combination of MATLAB modeling and experimental testing is used to assess the viability of this design.

Results show that this agrivoltaic design can provide 50.1% of the annual energy yield of a conventional non-tracking fully populated photovoltaic module and 64.73% of a previously evaluated non-tracking holographic planar concentrator photovoltaic module. Although the agrivoltaic design provides a lower annual energy yield than other photovoltaic (PV) systems, much of the solar radiation is incident onto the crop area below the module. The design maximizes the daily energy yield during the winter and summer. During these time periods,

cascaded gratings efficiently diffract light to their respective PV cells. This results in a dip in the amount of energy reaching the crop area for 5 hours in the winter and 2 hours in the summer centered at noon. This design allows for the available photosynthetically active radiation (PAR) during sunrise and sunset to be incident onto the crop when the available PAR is lower than the saturated PAR for the crop. Additionally, the design diffracts a fraction of the available PAR to the PV cell around noon when the available PAR can exceed the crop needs and become saturated, reducing plant growth.

Chapter 1: Defining the Problem

1.1: A Growing Population and an Increased Demand for Food and Energy

There is a growing demand for both food and energy to satisfy the needs of the ever-increasing human population. The current world population is just under 7.9 billion people, a doubling in just the past 40 years. Although the yearly growth rate has decreased from 1.77% to 1.05% over this time, the world's population is projected to reach 9 billion by 2037 and 10 billion by 2057. The growing population directly results in an increased demand for both food and energy [1].

In 2005, agriculture use accounted for approximately 38% of the global land area. With current population growth projections and to maintain current food consumption levels, agriculture will need an area equivalent to 1/2 of the current terrestrial land area by 2030 and 2/3 of the current terrestrial land area by 2070 [2]. In addition to the increase in the land area needed to satisfy these predictions, water uptake for irrigation will also need to increase [2].

In addition to the growing demand for food, the annual projection published by the International Energy Agency also indicates that global energy demands will continue to increase as populations grow and poverty decreases. The world energy demand is projected to increase by 30% by the year 2040 [3].

1.2: Introduction to Agrivoltaics: A Potential Solution to the Growing Demand for Food and Energy

The growing demand for both food and energy encourages the development of potential solutions to these problems. Agrivoltaics is one such possible solution that has gained momentum in recent years. Agrivoltaics is the colocation of agriculture and photovoltaic energy systems in an attempt to solve the vulnerabilities of food, energy, and water systems by creating

a hybrid infrastructure for land use. However, the colocation of agriculture and photovoltaics does not come without unique challenges and difficulties to overcome.

Chapter 2: Photovoltaics

This chapter discusses some of the reasons for the increasing importance of photovoltaics as an energy source. It will also discuss some of the reasons that solar energy has yet to account for a significant portion of the Earth's produced electricity. In addition, some basic properties of solar illumination and solar cells will be discussed.

2.1: Need for Solar Energy

Photovoltaic cells convert solar energy directly into electricity. PV can revolutionize the world we live in, as sunlight is an effectively unlimited, clean, and renewable energy source. According to Ritchie, as of 2019, 84.3% of the world's energy comes from fossil fuels such as coal, natural gas, and oil [4]. Nuclear energy supplies another 4.3% of consumed energy [4]. Remaining uranium reserves can provide $2.5 * 10^{24}$ joules of energy [3] and remaining fossil fuel reserves are estimated to provide $0.4 * 10^{24}$ joules of energy using current extraction methods [3]. This amount can increase to $3.0 * 10^{24}$ if all existing methane is extracted [3]. In addition to the limited amount of energy that can be produced with the remaining uranium and fossil fuel reserves is the problem of their deleterious effect on the Earth's environment. The burning of fossil fuels produces carbon dioxide (CO_2), which contributes to the natural greenhouse effect of the atmosphere. According to [5], fossil fuel combustion is the most significant human influence on climate, accounting for 80% of greenhouse gas emissions. These emissions have already had and will continue to have drastic impacts on the Earth's climate. Examples include irregular weather patterns, melting ice caps leading to increased coastal flooding, and alterations in precipitation and storm cycles [5]. Nuclear energy is an alternative resource used as a source of thermal and electrical energy [6]. However, it also has associated risks such as drastic negative environmental impacts due to the radioactive waste byproducts of

nuclear energy and due to the consequences of uranium mining [6]. There is also the risk of deadly and costly nuclear disasters.

Despite the finite amount available and the negative impacts and risks associated with fossil fuels and nuclear energy, these two energy sources still account for 88.6% of the supplied energy to the world. Renewable energy accounts for the remaining 11.4% of the supplied energy [4]. Of the 11.4%, only 1.1% is solar energy [4]. Solar radiation hitting the Earth can provide $3.8 * 10^{24}$ joules/year of energy [3]. Therefore, if only 0.1% of the Earth's landmass is used for solar collection with systems that are only 10% efficient, the current energy needs of the Earth's population could be fully met [7]. Solar energy accounts for only 1.1% of the Earth's produced energy because photovoltaic modules have historically been quite expensive. The cost of photovoltaic modules has decreased by a factor of approximately 15 over the past decade [8]. This has further led to a decrease in the levelized cost of photovoltaic-generated electricity [8]. Two reasons for this are a reduction in manufacturing costs and an increase in module efficiency. Increasing the efficiency of modules can be done by increasing the photons incident on the solar cell or more efficiently converting the incident photons into electrical energy. Both methods can be achieved by strategically adding holographic optical elements into the module, as will be discussed in a later chapter.

2.2: Solar Illumination Properties

Because solar cells convert sunlight into electrical power, this section is devoted to a brief characterization of some properties of the sun. A layer of hydrogen ions near the sun's surface absorbs radiation from the center of the sun [7]. The outer layer, called the photosphere, then re-radiates this energy. A black body at a temperature of 5778K is a good approximation of the radiated energy from the photosphere [7]. A black body is both a perfect absorber and a

perfect emitter of radiation. The power emitted is a function of both wavelength and temperature. The wavelength at which the peak power is emitted decreases when the temperature increases. The majority of light radiating from the sun is ultraviolet, visible, and infrared light and reaches the Earth in approximately 8.3 minutes. As the sunlight passes through Earth's atmosphere, it is scattered and filtered by various molecules in the atmosphere, such as water vapor and carbon dioxide. These molecules are why there are windows or gaps in the solar irradiance spectrum reaching the Earth. Outside the Earth's atmosphere, the total solar flux integrated over all wavelengths is 1367 W/cm^2 [7]. Attenuation through the atmosphere reduces the irradiance to approximately 970 W/cm^2 [7]. Figure 1 shows the solar spectrum for extraterrestrial and direct illumination and the power emitted by a black body at a temperature of 5778 K.

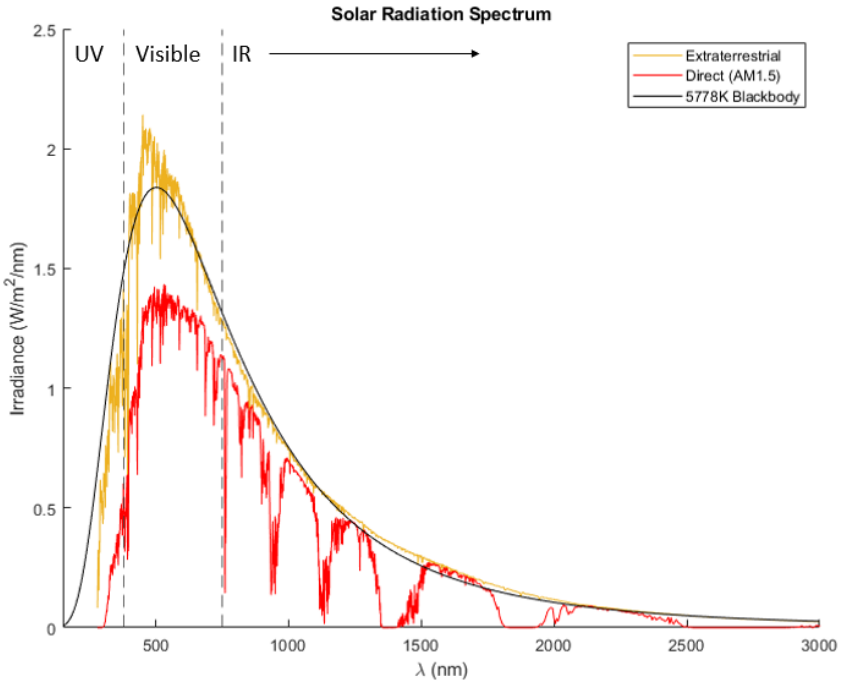

h

Figure 1: Solar Spectrum from wavelength 150-3000nm.

The irradiance from the sun reaching the Earth's surface is typically split into several components. Direct Normal Irradiance (DNI) is the measured irradiance illuminating a surface that is perpendicular to a ray from the sun. Diffuse Horizontal Irradiance (DHI) is the irradiance illuminating a horizontal surface from light scattered by the atmosphere. This measurement also includes circumsolar radiation (radiation that is forward scattered by the sun). Global Horizontal Irradiance (GHI) is the total irradiance illuminating a horizontal surface and includes direct, diffuse, and circumsolar. The DNI is multiplied by the solar zenith angle (θ_{zenith}) to account for radiation not at normal incidence to the surface. The equation that relates the three irradiance components is:

$$GHI = DHI + DNI * \cos(\theta_{zenith}) . \quad (2.1)$$

Cloud cover reduces the amount of solar illumination reaching the Earth's surface and produces variations in the illumination level over the course of a day. Clouds can block the direct sunlight from the sky; however, a portion of this light is recovered as diffuse scattered light.

2.3: Photovoltaic Cell Properties

The photovoltaic cell is the primary component of a photovoltaic system. Various semiconductor materials have been used in photovoltaic systems; the most common material is silicon (Si). Different forms of silicon, such as crystalline, multi-crystalline, and amorphous thin-film silicon, can be used to fabricate PV cells. The cost of silicon typically makes up about 40-60% of the overall cost of the PV system [9].

When silicon cells are illuminated, they produce an open circuit voltage of approximately 0.5 V and a short circuit direct current of 22-30 mA/cm^2. Cells are typically connected in series to increase the voltage for different applications. The output power varies throughout the day and is either connected to a storage device, such as a battery or to the electrical grid [9].

Semiconductors have energy levels: a conduction band and a valence band that are separated by a bandgap energy E_g [9]. The bandgap energy of silicon is $E_g(Si) = 1.12\ [eV]$. A photon has energy expressed in electron volts (eV) which is related to the wavelength in micrometers through the relationship:

$$E_{ph}(eV) = \frac{hc}{q\lambda} = \frac{1.24}{\lambda(\mu m)}\ [eV], \tag{2.2}$$

where *h* is Planck's constant, *c* is the speed of light in a vacuum, q is the charge of an electron, and λ is the photon's wavelength.

When a photon with less energy than the bandgap energy ($E_{ph} < E_g$), the material is transparent to that incident photon and the photon passes through the material. When a photon has energy greater than the bandgap energy, the photon is absorbed and transfers energy equal to the bandgap energy into an electron-hole pair. The energy transports the electron from the valence band to the conduction band [9]. Excess energy is converted into heat. When the photon has energy equal to the bandgap energy, the energy is most efficiently converted into a useful voltage. For silicon, the wavelength that corresponds to this condition is approximately 1100 nm.

The probability that a photon will be absorbed after propagating a distance *x* into a material and producing an electron-hole pair is equal to:

$$P(x) = \left[1 - \mathrm{e}^{-\alpha(\lambda)x}\right], \tag{2.3}$$

where α is the absorption of the material and is a function of the wavelength of the incident photon.

A p-n junction separates the electron and hole carriers in a solar cell to create a voltage. P-n junctions are formed by joining an n-type material (high electron concentration) to a p-type material (high hole concentration). Electrons diffuse from the n-type material to the p-type material and likewise for the holes from the p-type material to the n-type material. When the

electrons and holes move across the junction, they leave behind exposed charged dopant atom sites. On the n-type side, positive ion cores are exposed, and on the p-type side, negative ion cores are exposed. An electric field forms between the positive and negative ion cores that sweeps carriers out of the region. This region is depleted of free carriers and is thus called the depletion region. When an incident photon has energy greater than the bandgap energy, the photon is absorbed and creates an electron-hole pair. When the photon is absorbed within or near the depletion region electrons are swept across the junction to the n-side and holes to the p-side. Electrons then move through the load resistance producing power and recombine with holes at the rear contact (see Figure 2) [9].

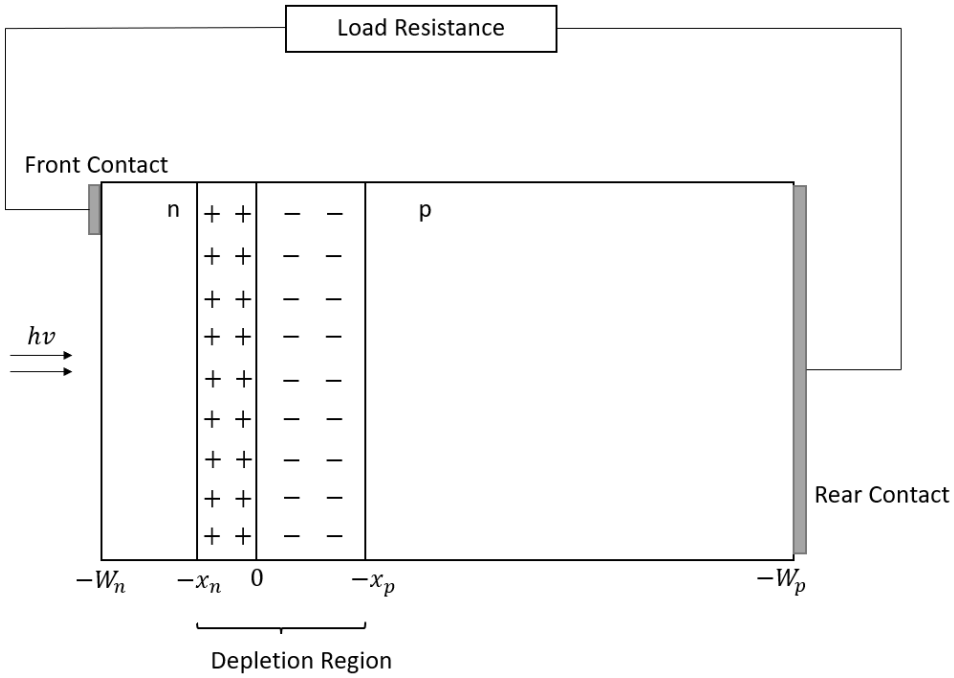

Figure 2: P-n junction diode schematic.

Light absorbed in the depletion region most efficiently produces a useful current. The probability that a photon will be absorbed within the depletion region is:

$$P = \left[1 - e^{-\alpha_n(\lambda)x_n - \alpha_p(\lambda)x_p}\right]. \quad (2.4)$$

The equivalent circuit for an ideal PV cell is illustrated in Figure 3. The circuit consists of a current source in parallel with a diode. The output of the current source is a function of the incident illumination. The current from the current source is divided between the diode and the load resistance. The diode equation is an expression of the current through a diode and is a function of voltage:

$$I_{diode} = I_0\left(e^{\frac{qV}{mk_BT}} - 1\right), \tag{2.5}$$

where I_{diode} is the current flowing through the diode, I_0 is the dark saturation current, q is the charge of an electron, V is the voltage across the diode junction set by the load impedance, m is the ideality factor that ranges from 1-2, k_B is Boltzmann's constant, and T is the temperature in Kelvin.

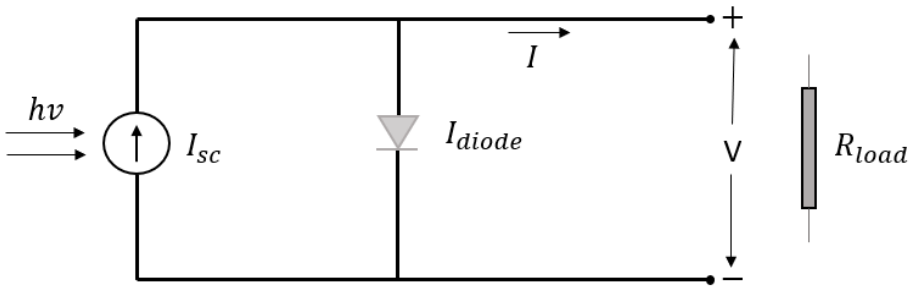

Figure 3: Equivalent circuit for an ideal PV cell.

The current through the load resistance is given by:

$$I = I_{sc} - I_0\left(e^{\frac{qV}{k_BT}} - 1\right). \tag{2.6}$$

The open circuit voltage (V_{oc}) is obtained when the load is an open circuit (infinite resistance) and is given by:

$$V_{oc} = \frac{mk_BT}{q}\ln\left(\frac{I_{sc}}{I_0} + 1\right). \tag{2.7}$$

The short circuit current (I_{sc}) is obtained when the load is shorted and is given by:

$$I_{sc} = qA_{pv}\int_{E_{BG}}^{\infty} b_s(E_{ph})\eta_{ext}(E_{ph})dE_{ph}\,, \tag{2.8}$$

where $b_s(E_{ph})$ is the incident photon flux density, η_{ext} is the PV cell's external quantum efficiency, and E_{ph} is the photon energy. For an intermediate load resistance (R_L) the voltage will vary from 0 and V_{oc} [9]. The current and voltage are functions of the illumination and load condition. The output current is proportional to the illumination area. A current-voltage (IV) curve, shown in Figure 4, can be used to determine how much power a solar cell will produce. The maximum power output (P_{MP}) occurs at an optimum current I_{MP} and a voltage V_{MP} value [11]. V_{MP} can be computed from the derivative of *IV* with respect to *V* and setting the resulting expression to zero:

$$V_{MP} = V_{oc} - \frac{mk_BT}{q}\ln\left(\frac{V_{MP}}{mk_BT/q} + 1\right). \tag{2.9}$$

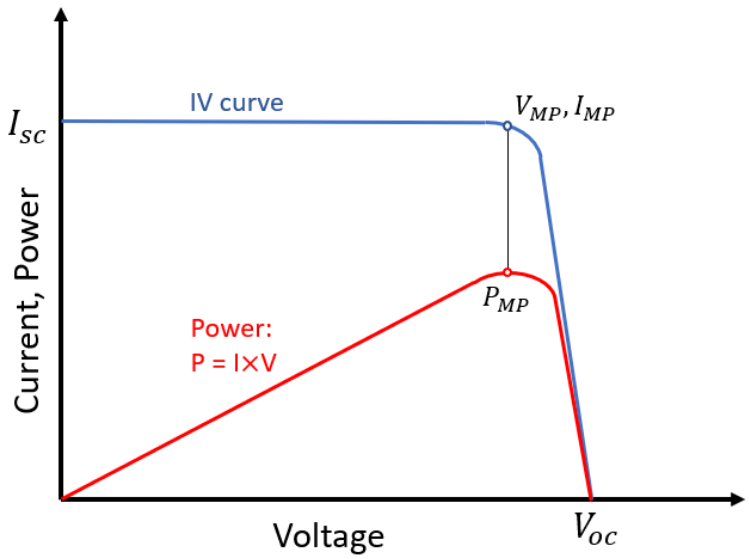

Figure 4: IV curve of a solar cell. The maximum power output P_{MP} of the solar cell occurs at a voltage V_{MP} and a current I_{MP} [11].

The Fill Factor (FF) is a measure of the electrical efficiency of a cell and is given by the ratio:

$$FF = \frac{V_{MP} I_{MP}}{V_{oc} I_{sc}}. \tag{2.10}$$

Therefore, if the *FF*, V_{oc}, and I_{sc} are known, the maximum power can be readily determined:

$$P_{MP} = V_{oc} I_{sc} FF. \tag{2.11}$$

The power conversion efficiency of the solar cell is the fraction of the incident optical power converted into electricity:

$$\eta = \frac{V_{oc} I_{sc} FF}{P_{inc}} \tag{2.12}$$

The internal quantum efficiency (η_{int}) is the probability that an incident photon within the material with wavelength λ forms an electron-hole pair and is given by:

$$\eta_{int} = \exp[-\alpha_n (W_n - x_n)] \left[1 - \exp\left(-\alpha_n x_n - \alpha_p x_p\right)\right]. \tag{2.13}$$

The external quantum efficiency (η_{ext}) is the probability that an incident photon will deliver an electron to an external circuit. This accounts for the optical power loss when coupling light into the cell. The external quantum efficiency is a function of the internal quantum efficiency and is given by:

$$\eta_{ext}(\lambda) = (1 - R) s F_m \exp[-\alpha_n (W_n - x_n)] \left[1 - \exp\left(-\alpha_n x_n - \alpha_p x_p\right)\right], \tag{2.14}$$

where *R* is the percentage of incident power reflected from the surface of the PV cell, *s* is the grid shadow factor, and F_m is a material factor that accounts for other effects that degrade conversion efficiency.

The Spectral Response (SR) is another valuable parameter for evaluating the performance of a PV cell. The units of the SR are current out over the optical power illuminating the cell (A/W) and is related to the external quantum efficiency by:

$$SR(\lambda) = \frac{q\lambda}{hc}\eta_{ext}(\lambda). \tag{2.15}$$

The ideal and measured SR of a silicon cell are shown in Figure 5.

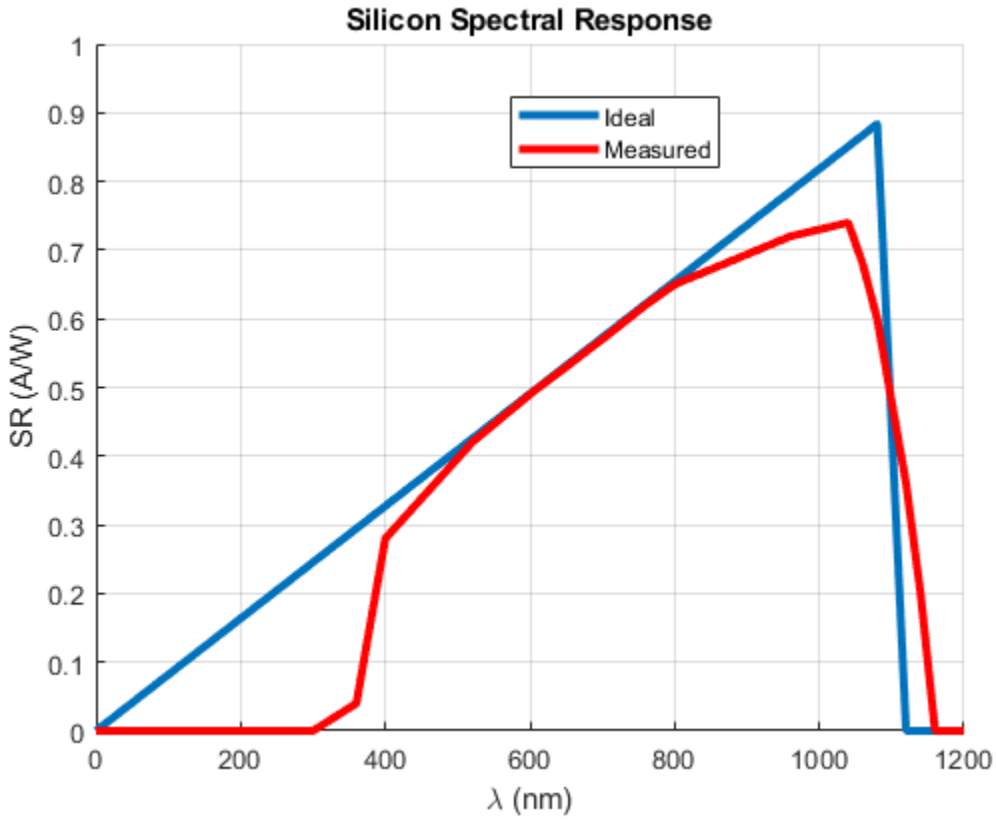

Figure 5: The ideal (blue) and measured (red) spectral response of a silicon cell. At short wavelengths, surface recombination effects decrease SR. Longer wavelengths corresponding to photons with energy less than the bandgap energy do not supply enough energy to create an electron-hole pair, and thus, the spectral response falls to zero. Silicon is an indirect bandgap semiconductor and requires momentum from a lattice vibration in order for a transition to take place. This tends to decrease the sharpness of the cut-off near the band edge [12].

Chapter 3: Agrivoltaics

3.1: Photosynthetically Active Radiation

As described in the previous chapter, the solar radiation incident on a PV cell within the spectral response range of the PV cell is converted into electrical energy. Likewise, crop productivity depends on the radiation conversion efficiency, which is the efficiency of converting the photosynthetically active radiation (PAR) into plant biomass [13]. Different crops efficiently convert varying spectral bandwidths into plant biomass; however, for the remainder of this report the PAR explicitly refers to the spectral bandwidth between 400-700 nm that is available for photosynthesis. This is a commonly cited spectral bandwidth for the PAR region.

The colocation of solar photovoltaics and agriculture demands careful consideration of sharing solar illumination between the PV system and the crops to ensure optimal efficiency for both food and energy production. Around noon, available PAR can exceed what the crop needs [13]. The available PAR is lower during sunrise and sunset than the optimum PAR irradiance for plants [13]. Optimally, designs should ensure that the PAR irradiance available to the crops remains close to the crop required PAR and allows excess radiation to be collected by the PV arrays [13].

3.2: Synergistic Benefits

A study performed by the University of Arizona in Tucson shows that the colocation of agriculture and photovoltaics could synergistically support ecosystem services such as crop production, local climate regulation, water conservation, and renewable energy production [14]. Although the plants growing under photovoltaic systems receive less light than traditional agricultural systems, this could be beneficial, as there is also reduced evaporative loss of soil moisture in dryland areas. In this study, certain crops have been shown to increase fruit

production and CO_2 uptake. Additionally, the transpirational water loss has created an energy balance shift towards latent heat exchange and less sensible heat flux to the atmosphere, resulting in significantly cooler photovoltaic modules in the daytime. This would contribute to increased energy production by reducing cell temperature and increasing voltage output [14].

The benefits of agrivoltaics are maximized in hot and arid climates when shading can be utilized to support a healthier water balance. In addition, agrivoltaics could allow for the restoration and revegetation of degraded and arid areas. Conventional agrivoltaic designs can reduce the solar radiation reaching the crops by about one-third, so the effectiveness of agrivoltaics is dependent on the shade tolerance of the crops [15]. Additionally, agrivoltaics enhances the value of farmland and can provide off-grid electricity in rural and developing areas. The colocation of agriculture and photovoltaics can increase land productivity by up to 70% [16].

3.3: Dual use of the Solar Spectrum

As discussed earlier, a critical design criterion for an agrivoltaic model is to effectively split the solar spectrum to ensure optimal plant growth while redirecting excess solar radiation onto the PV system. Currently, most reported research analyzes systems that consider various orientations and positions of PV collection systems above the crop area or using tinted semi-transparent solar modules. Another methodology is to use optical elements that manipulate the solar spectrum such that the PAR irradiance is incident on the crop area and the remaining spectral components illuminate the PV system. The following two subsections on dichroic film and holographic optical elements discuss this proposed methodology further.

3.3.1: Dichroic Material

Dichroic film is an optical material used to selectively transmit or reflect light within a range of wavelengths. A potential design can be seen in Figure 6. The solar spectrum (300-4000 nm) is incident onto the dichroic film such that the PAR (400-700 nm) band is transmitted through the dichroic film and goes to the crop area, whereas other wavelengths are reflected toward the PV cell.

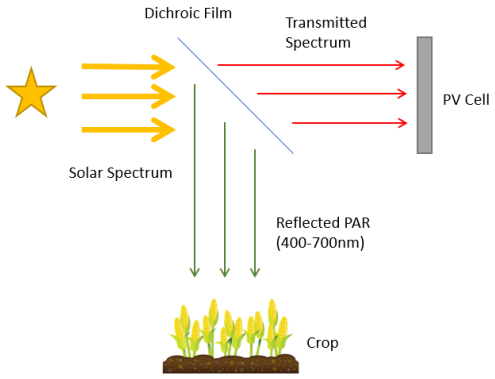

Figure 6: An agrivoltaic system where a dichroic filter is used to split the solar spectrum.

Figure 7 shows results experimentally obtained measuring the spectral transmittance of 3M Blazed type dichroic film [17] for various degrees of incident light. At normally incident light, the dichroic film efficiently reflects light between 600 nm and 800 nm. Below 600 nm and above 800 nm, the light is transmitted at approximately 90% efficiency. As the angle of incidence increases, the spectral bandwidth of reflected light shifts to lower wavelengths. Dichroic film can also be designed to transmit a spectral band with similar efficiencies instead of reflecting a spectral band, as shown in Figure 7. Due to this spectral shift, solar tracking would be an important design consideration to ensure optimal illumination conditions.

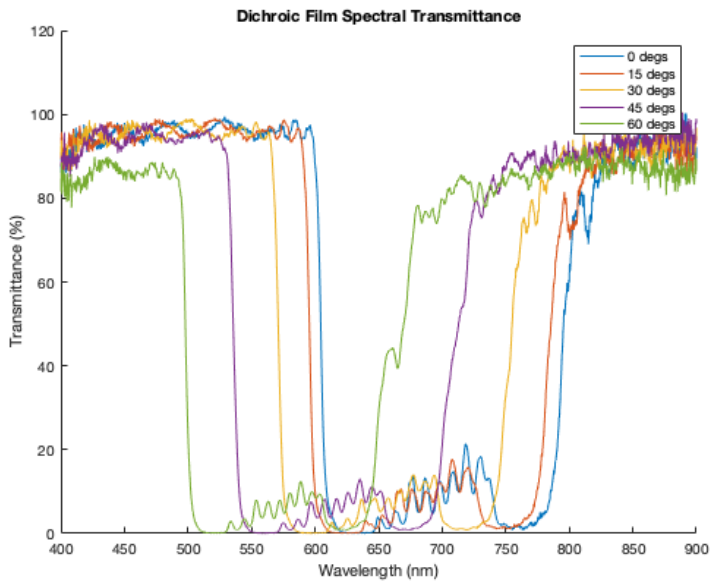

Figure 7: Spectral transmittance of 3M dichroic blazed film at various angles of incidence.

3.3.2: Holographic Optical Elements

Holographic optical elements can also be used to split the solar spectrum. Holograms have a property known as chromatic selectivity, which means that different portions of an incident light source's spectrum will more efficiently diffract depending on the hologram properties and the angle of incidence of light onto the hologram. The condition which describes the hologram's maximum diffraction efficiency is known as the Bragg condition, and the diffraction efficiency decreases as reconstruction parameters deviate from this condition. The next chapter goes more into depth on holographic optical elements. Theoretically, holographic optical elements can be constructed such that the wavelengths of light that the PV cell are sensitive to diffracts onto the PV system and allows for the PAR spectral bandwidth to transmit toward the crop area. Chapter 7 analyzes a novel agrivoltaic design that diffracts light towards the PV area and transmits the remaining light to the crop area.

Chapter 4: Overview of Holography

4.1: Basics of Holography

Holography is a technique in which a wavefront is recorded onto a photosensitive material and then later reconstructed. It allows a 3D image to be encoded on a 2D plane and is accomplished by recording interference patterns (fringes) onto the photosensitive material. The holographic recording and reconstruction process consists of three steps: (1) superimposing coherent object and reference beams to form an interference pattern; (2) exposing a photosensitive recording material to the interference pattern capturing the amplitude and phase information of the object light; and (3) reconstructing the holographic image [16]. A holographic optical element (HOE) refers to a hologram that converts an incident wavefront into an output wavefront. Examples of this include using a hologram to replace a conventional lens, mirror, polarizer, or filter. A planar holographic grating is formed when both the reference and the object beams are collimated and superimposed onto the recording material. A typical setup for recording a planar transmission hologram is shown in Figure 8.

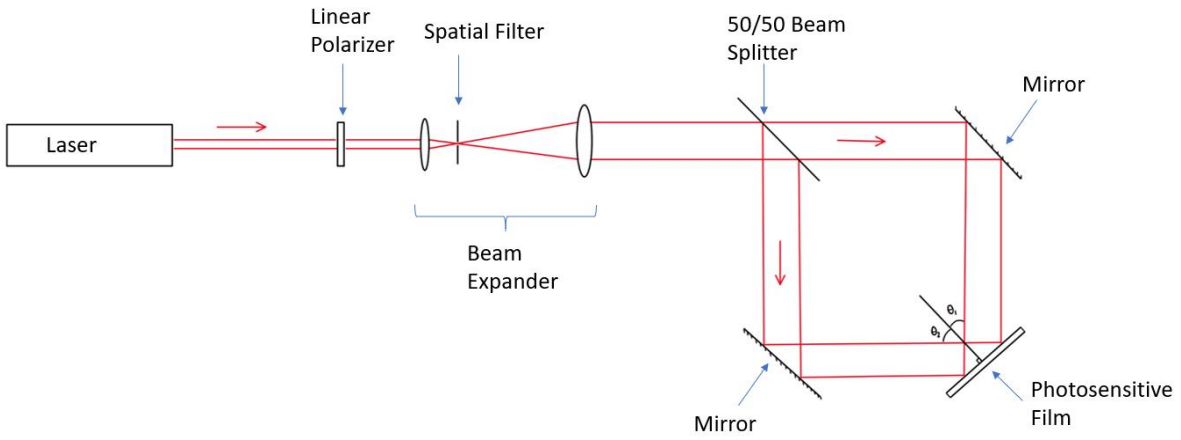

Figure 8: Optical setup for recording holographic transmission gratings. The laser light goes through a linear polarizer that vertically polarizes the light, which then travels through a beam

expander, increasing the beam's radius. At the focal point of the beam expander is a spatial filter that is used to remove aberrations. The beam then passes through a 50/50 beam splitter separating the beam into a reference and an object beam. These two beams then interfere at the plane of the photosensitive film, thus creating an interference pattern that is recorded onto the film.

The resulting interference fringe pattern that is recorded in the material is made up of parallel planes of constant phase with grating period Λ, and grating vector $\vec{K}$.

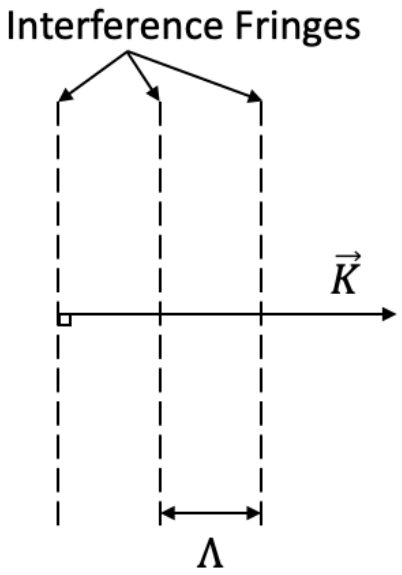

Figure 9: Recorded interference fringes with grating vector $\vec{K}$ and grating period Λ [19].

The grating vector is the vector perpendicular to the interference fringes, as shown in Figure 9. It is equal to the difference between the two propagation vectors that form the holographic grating and is given by Equation 4.1:

$$\vec{K} = \overrightarrow{k_1} - \overrightarrow{k_2}. \tag{4.1}$$

The direction of the propagation vectors is defined by the angles relative to the optical axis, typically the +z direction. In the x-z plane, the resultant propagation vectors are:

$$\overrightarrow{k_1} = \frac{2\pi}{\lambda_1/n}\sin(\theta_1)\,\hat{x} + \frac{2\pi}{\lambda_1/n}\cos(\theta_1)\,\hat{z}, \tag{4.2}$$

$$\overrightarrow{k_2} = \frac{2\pi}{\lambda_1/n}\sin(\theta_2)\,\hat{x} + \frac{2\pi}{\lambda_1/n}\cos(\theta_2)\,\hat{z}, \tag{4.3}$$

where λ_1 is the wavelength of the recording beams, n is the refractive index of the material in which the beam propagates, and $\theta_{1,2}$ are the angles that the propagation beams make with the z-axis. The magnitude of the grating vector is given by:

$$\left|\vec{K}\right| = \frac{2\pi}{\Lambda}\,, \tag{4.4}$$

where Λ is the grating period.

The diffraction efficiency is the amount of optical power diffracted into a particular order relative to the power incident on the hologram and is equal to:

$$\eta_q = \frac{P_q}{P_{inc}}, \tag{4.5}$$

where P_q is the optical power diffracted into the qth order and P_{inc} is the power incident onto the hologram. Equation 4.1 is the Bragg condition for a volume grating and can be used to determine the reconstruction parameters that result in the maximum diffraction efficiency. The Bragg Circle Diagram is a useful graphical representation for evaluating various reconstruction conditions. The radius of the Bragg circle is equal to the magnitude of the construction propagation vectors, $k = \frac{2\pi}{\lambda/n}$, and the resultant grating vector remains fixed after the hologram is recorded. If reconstruction is done using a different wavelength, the length of the propagation vectors will change. In that case, for Bragg matching, the orientation and angles of the propagation vectors must change, as shown in Figure 10. In this Figure, the original construction vectors are $\vec{k}_{1,1}$ and $\vec{k}_{1,2}$, and forms the grating K-vector, $\vec{K}$. Upon reconstruction with a different wavelength, the propagation vectors become $\vec{k}_{2,1}$ and $\vec{k}_{2,2}$. In order to ensure that the Bragg

condition is satisfied at a different wavelength, the angles and orientations of the propagation vectors must change.

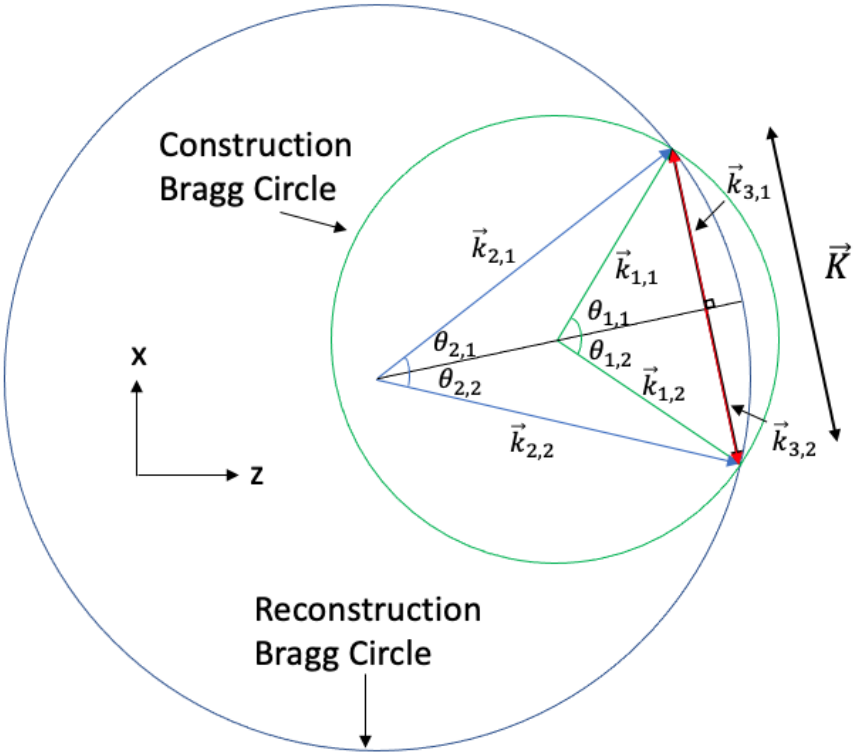

Figure 10: Bragg circle illustration showing Bragg matched conditions at different wavelengths and propagation vectors [19].

If the Bragg condition is not satisfied, which often occurs with solar illumination due to the sun's motion and broad spectrum, the diffraction efficiency of the holographic volume grating decreases from its maximum value. This case is illustrated using the Bragg circle diagram in Figure 11. When the reconstruction vector deviates from the Bragg condition, one or both ends of the K-vector no longer touch the circle, which can be interpreted as a deviation or detuning from the Bragg condition. The amount of deviation can be quantified using the detuning parameter, ϑ, and is defined as:

$$\vartheta = \frac{\beta^2 - |\sigma|^2}{2\beta}\,, \tag{4.6}$$

where β is the magnitude of the reconstruction propagation vector and $\vec{\sigma}$ is the diffracted beam propagation vector satisfying the Bragg condition, as shown in Equation 4.9. As this parameter increases, the diffraction efficiency decreases.

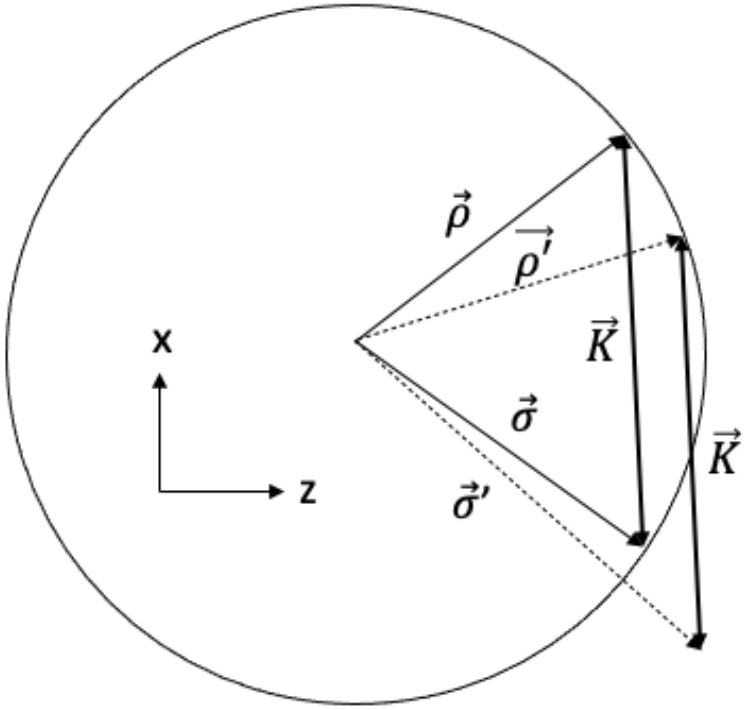

Figure 11: Bragg circle illustration showing a deviation from the Bragg matched condition [19].

There has been growing interest in the use of HOEs for solar energy applications due to the HOE's low production costs and potential for improving the efficiency of the photovoltaic system. Volume phase HOEs prove to be the most promising holographic type for this application due to their high efficiency, as well as their chromatic and angular selectivity [20]. These characteristics are functions of the construction parameters such as the recording geometry and photosensitive material properties.

4.2: Diffraction Efficiency Model (ACWA) & Verification

Coupled wave analysis is a valuable method for modeling the diffraction efficiency of a volume hologram. Coupled wave analysis can be divided into two categories: rigorous and approximate methods. Approximate models impose restrictive assumptions; however, they give close approximations to experimental results when the assumptions are satisfied. Kogelnik's Approximate Coupled Wave Analysis (ACWA) is a commonly used approximate analytical model that is relatively easy to integrate into an optical simulation model. The primary assumption of this model is that only the reconstruction wave and one diffracted wave have significant magnitude. The model can be modified to 3 spatial dimensions to describe out-of-plane incidence under certain conditions [21].

At a construction wavelength λ_{con}, the grating vector is given by:

$$\vec{K} = \begin{bmatrix} K_x \\ K_y \\ K_z \end{bmatrix} = \frac{2\pi n}{\lambda_{con}} \begin{bmatrix} \sin(\theta_{con})\sin(\phi_{con}) - \sin(\theta_{ref})\sin(\phi_{ref}) \\ \sin(\theta_{con})\cos(\phi_{con}) - \sin(\theta_{ref})\cos(\phi_{ref}) \\ \cos(\theta_{con}) - \cos(\theta_{ref}) \end{bmatrix}, \tag{4.7}$$

where θ_{con} and θ_{ref} are the construction and reference beam zenith angles in the grating material, ϕ_{con} and ϕ_{ref} are the construction and reference azimuthal angles in the grating medium, and n is the mean refractive index of the grating medium.

At a reconstruction wavelength λ_{rec}, the propagation vector for the incident beam is given by:

$$\vec{\rho} = \begin{bmatrix} \rho_x \\ \rho_y \\ \rho_z \end{bmatrix} = \beta \begin{bmatrix} \sin(\theta_{rec})\sin(\phi_{rec}) \\ \sin(\theta_{rec})\cos(\phi_{rec}) \\ \cos(\theta_{rec}) \end{bmatrix}, \qquad \beta = \frac{2\pi n}{\lambda_{rec}} \tag{4.8}$$

where θ_{rec} and ϕ_{rec} are the incident zenith angle and azimuthal angle for reconstruction. The corresponding diffracted beam propagation vector for a given incident beam is

$$\vec{\sigma} = \vec{\rho} - \vec{K} . \tag{4.9}$$

Volume transmission phase gratings have minimal absorption and thus can achieve the highest diffraction efficiency making this type of holographic grating optimal for an agrivoltaic application. For a transmission phase grating, the diffraction efficiency is given by:

$$\eta = \frac{\sin^2\left(\sqrt{\nu^2 + \xi^2}\right)}{1 + \frac{\xi^2}{\nu^2}} . \tag{4.10}$$

The parameter ν determines the maximum diffraction efficiency of the grating for a specific refractive index modulation, thickness, reconstruction wavelength and angle. The parameter ξ indicates the variation of the reconstruction parameters from the Bragg condition.

$$\nu = \frac{\pi n_1 d}{\lambda_{rec}\sqrt{c_r c_s}} . \tag{4.11}$$

$$\xi = \frac{\vartheta d}{2c_s} . \tag{4.12}$$

The parameter n_1 is the refractive index modulation of the hologram, d is the thickness of the hologram, and ϑ is the detuning parameter. The additional constants c_r and c_s are given by:

$$c_r = \frac{\rho_z}{\beta} , \tag{4.13}$$

and

$$c_s = \frac{\sigma_z}{\beta} . \tag{4.14}$$

Lastly, the diffraction angle of the holographic grating is determined using the grating equation given by:

$$\begin{bmatrix} \sin\left(\theta_{i,xz}\right) - \sin\left(\theta_{d,xz}\right) \\ \sin\left(\theta_{i,yz}\right) - \sin\left(\theta_{d,yz}\right) \end{bmatrix} = \begin{bmatrix} -\frac{\lambda_{rec}}{\Lambda_{xz}} \\ -\frac{\lambda_{rec}}{\Lambda_{yz}} \end{bmatrix}, \tag{4.15}$$

where θ_i is the angle of incidence in either the x-z or y-z plane for the incoming illumination, θ_d is the angle that the illumination will be diffracted in the x-z or y-z plane, λ_{rec} is the reconstruction wavelength, and Λ is the grating period in the x-z or y-z plane.

The dispersion factor (DF) is a measure of the change in ray angle emerging from a grating as a function of the change in wavelength:

$$DF = \frac{\Delta\theta}{\Delta\lambda}. \tag{4.16}$$

For a thin grating, the grating equation (Equation 4.15) is used to derive the DF:

$$\frac{\Delta\theta}{\Delta\lambda} \approx \frac{1}{\cos(\theta_{diff})\,\Lambda}. \tag{4.17}$$

For a volume grating, the derivation of the DF is more involved:

$$\frac{d\theta}{d\lambda} = \frac{1}{2n\Lambda\sin(\phi - \theta)}, \tag{4.18}$$

where *n* is the mean refractive index in the grating medium, ϕ is the angle of the grating vector with respect to the z-axis, and θ is the incident angle of the reconstruction beam.

In order to validate the Kogelnik ACWA model, a holographic grating is recorded in Covestro HX200 photopolymer film using collimated beams at incident angles of 15° and -29.5°, in air, with respect to the hologram surface normal and a construction wavelength of 457 nm illuminating the hologram with a combined exposure illumination of 2.0 $\frac{mW}{cm^2}$. Different durations of exposures were tested to determine the exposure energy that would result in maximum diffraction efficiency. A four-second exposure corresponding to an exposure energy of 8 $\frac{mJ}{cm^2}$ resulted in the maximum diffraction efficiency and was used for the remainder of this experimental verification. The thickness of Covestro is 16 μm, it has an average refractive index of 1.5, and has a rated maximum index modulation of 0.03. However, using the recording

parameters detailed above, the index modulation that resulted in the maximum diffraction efficiency was 0.012 as shown by Figure 12 a). The measured diffraction efficiency for this grating is shown in Figure 12 b). There was good agreement between the simulated results (blue line) and the experimental results (orange line).

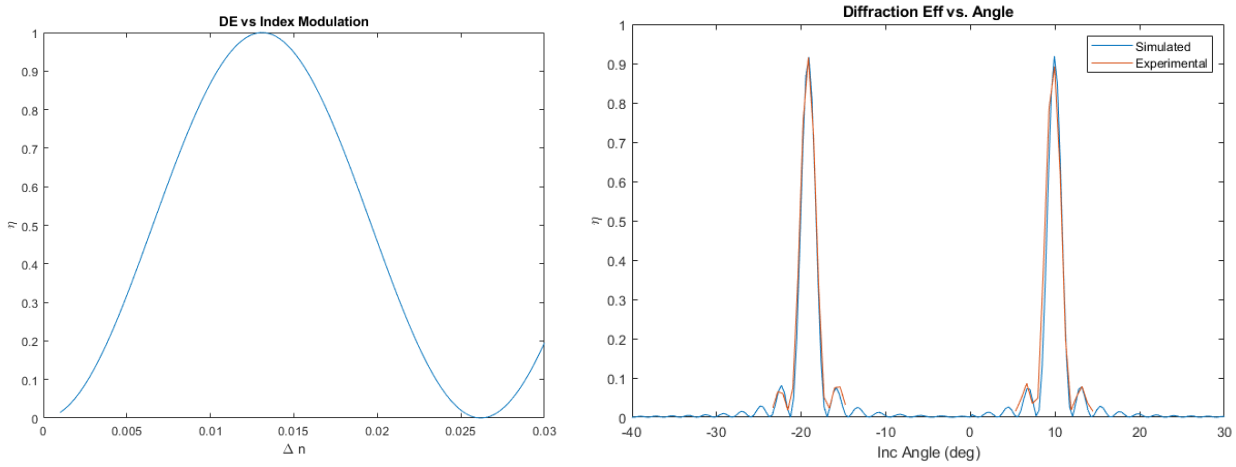

a) b)

Figure 12: Simulated (blue line) and Experimental (orange line) diffraction efficiency as a function of in-plane incident angle. The incident angle is given in the material and was found using Snell's Law.

4.3: Chromatic Selectivity

Chromatic selectivity refers to a hologram being wavelength selective, meaning light diffracts efficiently for wavelengths that satisfy or nearly satisfy the Bragg condition and diffract less efficiently for wavelengths that deviate from the Bragg condition, as was discussed in Section 4.1. The spectral bandwidth of the diffraction efficiency as a function of the wavelength curve depends on the spatial period of the interference pattern and the thickness of the material [20]. The spectral bandwidth decreases as the inter-beam angle (the angle between the two beams) increases. This characteristic can be utilized to design HOEs that efficiently diffract

bandwidths of light that are most effectively converted into electricity for a given photovoltaic cell. Additionally, chromatic selectivity makes it possible to eliminate unwanted wavelengths (wavelengths that are not efficiently converted into electricity for a given photovoltaic cell) that can lead to overheating and a decrease in energy conversion efficiency of a photovoltaic cell. In an agrivoltaic setting, this characteristic can also be used to diffract a desired spectral range toward the PV cell while transmitting the rest of the spectrum toward the crop area.

4.4: Angular Selectivity

Angular selectivity refers to a hologram diffracting light more efficiently for a range of incident angles near the angle that satisfies the Bragg condition [20]. The angular selectivity is most sensitive when the angle of the incident illumination varies in the direction of the recording plane (i.e., perpendicular to the direction of the fringes). The angular selectivity is less sensitive in the plane parallel to the fringes, as shown in Figure 13. In photovoltaic applications, angular selectivity is typically an undesirable trait because the position of the sun varies throughout a given day and the year. In practice, the undesirable nature of this characteristic can be addressed by using solar tracking, multiplexed gratings, or cascaded holograms. Additionally, because angular selectivity differs in sensitivity depending on the plane of angle variation, it is possible to design photovoltaic systems that only require one-axis tracking to track the sun's height during the course of the day [20].

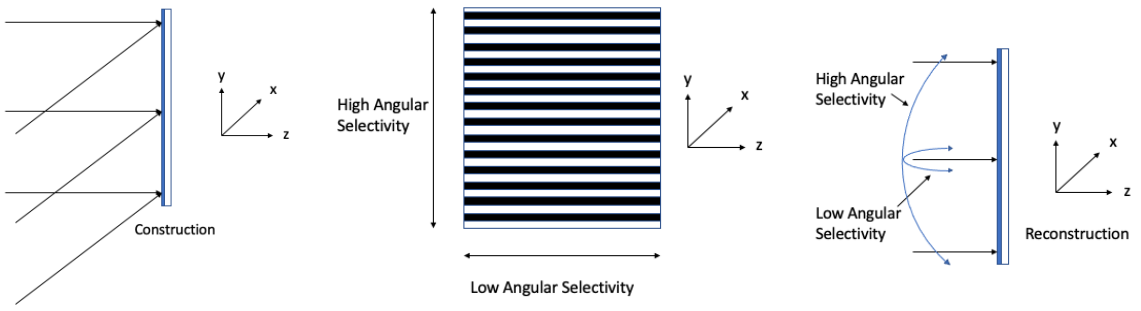

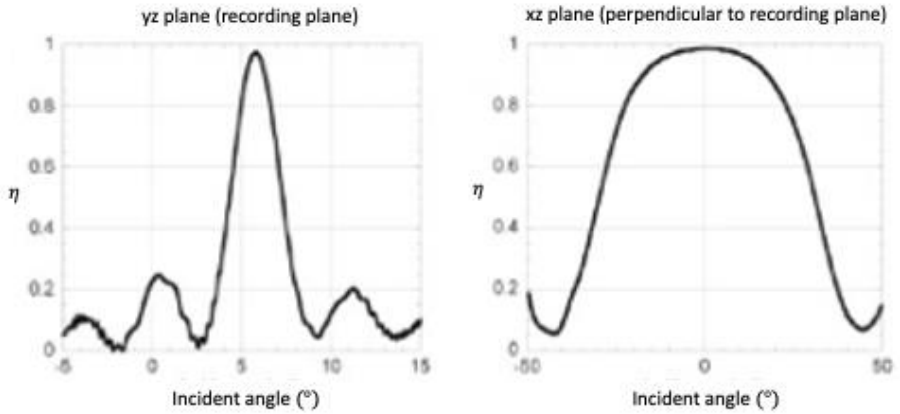

Figure 13: Illustration showing the orientation of the recording beams, the fringe pattern, and the planes of high/low angular selectivity. An example of DE as a function of incident angle for both planes is also shown [20].

4.5: Photosensitive Materials: Covestro vs. DCG

Two materials commonly used for manufacturing holographic optical elements are Covestro photopolymer and Dichromated Gelatin (DCG). DCG has been used for over 50 years to record volume phase holograms because it has excellent properties that allow for the inexpensive production of high diffraction efficiency holographic optical elements that are stable for a long time. Fundamental DCG properties include [22]:

1) uppermost refractive index modulation ($\Delta n \sim 0.1$),
2) ability to diffract light from the near UV to the mid-IR,
3) minimal scattering,
4) dimensionally molecular spatial resolution, meaning possessing the ability to store between a few hundred to several thousand lines per millimeter,
5) excellent resilience to temperature change and stability over multiple years,
6) sensitivity within the range of common laser wavelengths,

7) mean refractive index close to 1.5 reducing glass substrate reflections, and
8) inexpensive raw materials that can be purchased in large quantities.

DCG does have some drawbacks that make the material difficult to work with in an uncontrolled environment. DGC has a reputation for inconsistency that has driven many researchers, engineers, and companies away from using it. DCG is hygroscopic and particularly sensitive to environmental humidity during the film drying process [23]. To improve the repeatability of both the Bragg wavelength and diffraction efficiency, an environmentally controlled environment to keep temperature and relative humidity constant is required. In addition, DCG must be prepared prior to the recording process and requires chemical curing processing after the recording.

For these reasons, another material called Covestro Bayfol HX [24] photopolymer is often used in place of DCG for different applications. Bayfol has various advantageous characteristics such as good light sensitivity, low shrinkage, low detuning, and requires no chemical or thermal processing after recording. Additionally, this material is purchased in a state that only needs to be laminated to a glass substrate prior to the recording process and only requires photocuring after exposure. These two properties allow for more repeatable results than with DCG. This material has moderate refractive index modulation (0.03) and can also be purchased in large quantities [22].

Due to the repeatability issues with DCG, many proposed solar applications that incorporate HOEs have suggested using Covestro as the material as it is simpler to work with and can produce more consistent results. However, newly reported research shows that the repeatability of holograms formed in DCG of both the Bragg wavelength and diffraction

efficiency can be improved by nearly 10X by controlling the humidity during the drying process. This research is discussed in the following section.

4.6: Improving the Repeatability of the Spectral Bandwidth and Diffraction Efficiency of holograms formed in Dichromated Gelatin [23]

This section details the methodology of making holograms using DCG as the recording material. Additionally, as DCG has historically been proven to give inconsistent results, this section details an experiment that analyzes the effect of humidity during the drying process on the repeatability of holograms recorded in DCG. The DCG film for this trial is fabricated using a mold coating process with the process parameters listed in Table 1.

Table 1: DCG film fabrication parameters.

Deionized water	25 grams
Type-A 300 bloom gelatin	3 grams
Ammonium dichromate	0.5 grams
Gelling Temperature	13 ℃
Gelling time	45 minutes
Curing Time	24 hours

Initially, 300 bloom strength type-A gelatin is dissolved in deionized water in a 50℃ hot water bath. Next, the light-sensitive material, ammonium dichromate, is mixed into the solution until dissolved. A few drops of the gelatin mixture are placed on the mold, as shown in Figure 14. The DCG mold is formed on a glass substrate using layers of tape to control the thickness of the gelatin. For the experiment conducted, 7mil thick electrical tape is used to form the raised edges of the border around the glass substrate. Rain-X Water Repellant [25] is applied onto the glass mold to prevent the DCG film from sticking to the mold, encouraging the film to stick to the glass cover plate which serves as the DCG substrate. After placing the gelatin on the mold, a glass substrate is placed against the mold. This process forces excess gelatin mixture out of the

corner of the mold. The mold and substrate are held together on the edges by clips before being placed in a refrigerator set at a temperature of 13℃ for 45 minutes until the gelatin is firm. The mold and the substrate are then carefully separated, with the DCG film adhering to the glass cover plate.

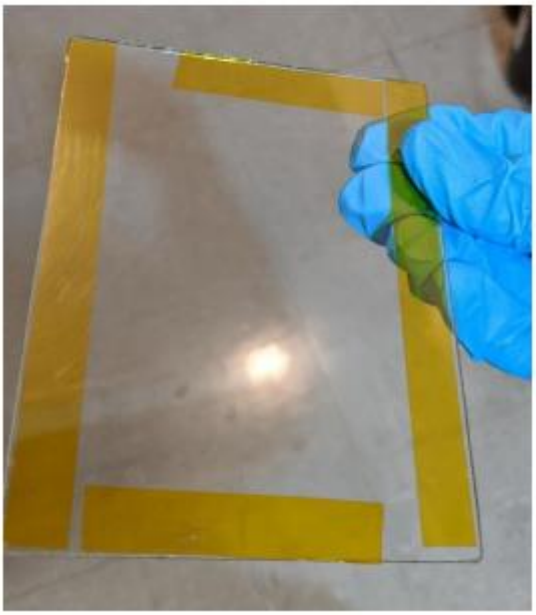

Figure 14: The DCG mold consists of 7 mil tape applied along the edges of a glass plate. Rain-X is applied onto the surface of the mold to prevent the film from sticking to the mold.

At this point, the DCG film still contains most of its initial water content and must be dried. The DCG film is placed in a "dry box" (dehumidifier) that contains a beaker of water to provide a locally controlled environment with adjustable humidity, as shown in Figure 15. The water in the beaker evaporates and is used to increase the humidity within the box. Once the target humidity is reached, the dehumidifier keeps the humidity constant. For this experiment, the humidity was controlled between 25% and 75% during the drying process. Airflow is also provided within the box by placing a fan beneath the DCG film. The film is left to dry in the dry box for 24 hours before recording the hologram. For the following study, six sets of holograms

were recorded with drying humidity levels of 25%, 35%, 45%, 55%, 65%, and 75%. For each set, multiple holograms were recorded using the same construction parameters. Recordings were made with a 457 nm laser, and the object and reference beams' recording angles were 8.9° and 29.5°, with respect to the surface normal of the film. The beam angles were selected to provide maximum diffraction efficiency for normally incident light at 600 nm after undergoing film swelling. It was found that the sensitivity to exposure energy density increased with higher curing humidity. For this reason, the exposure energy density was reduced for film cured at higher humidity levels to keep the diffraction efficiency similar for each set. For the sets with a drying humidity of 25% and 35%, an exposure energy density of 180 $\frac{mJ}{cm^2}$ was used. For the sets with a drying humidity of 45%-75%, an exposure energy density of 60 $\frac{mJ}{cm^2}$ was used. Each substrate was then cut into four pieces, and 2-3 holograms were recorded on each piece before the film was processed.

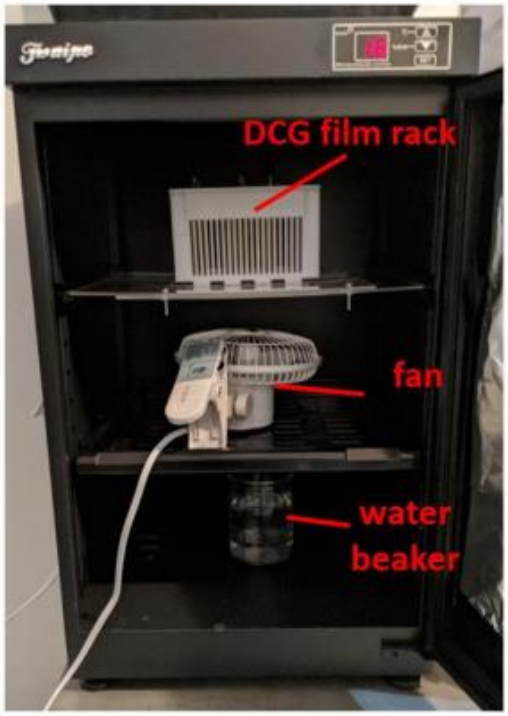

Figure 15: Humidity controlled "dry box" with the DCG film rack on top, a fan providing uniform airflow in the middle, and a water beaker providing an evaporative water source on the bottom.

The film was processed using a typical DCG processing procedure, as shown in Figure 16. After recording, the exposed DCG film was placed in a Kodak Rapid fixer bath. The fixing property of the bath helps to remove the dichromate from the null regions of the interference fringes. In addition, the hardening property of the bath increases the strength of the film to withstand the effects of rapid dehydration during successive baths of isopropyl alcohol (IPA). After the fixer bath, the film was placed in running water to wash away the weakened dichromate in the unexposed regions. The final three baths have increasing concentrations of IPA and are used to gradually dehydrate the swollen film. All solutions are at room temperature. After chemical processing, the film was dried using compressed air and placed in an oven set at 60°C for 15 minutes to remove any residual water content. The exposures and chemical processing were done in an uncontrolled environment where the room humidity varied from 20%-30% and the temperature varied from 27-29°C.

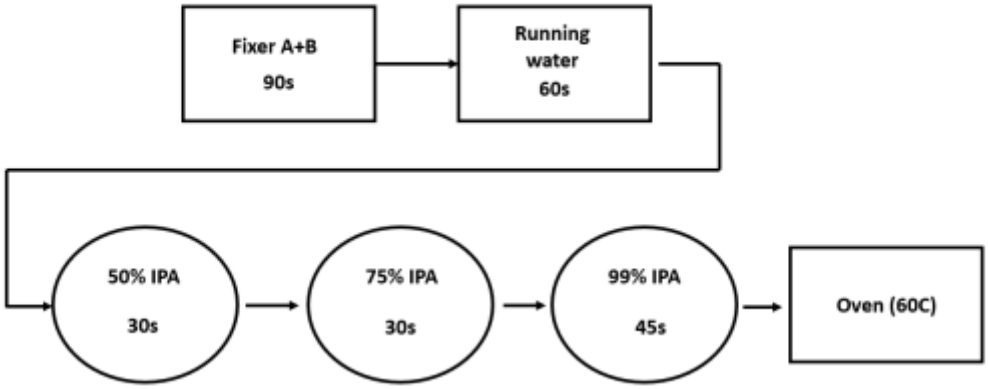

Figure 16: Flow diagram for DCG chemical processing.

The diffraction efficiency of each hologram was measured by evaluating the spectral transmittance. Light from a collimated broadband halogen lamp passes through the hologram at normal incidence. An optical fiber connected to an Ocean Optics 2000+ spectrometer was used to measure the spectral transmittance of the hologram. The measurements were normalized to the transmitted value through the glass substrate to account for Fresnel reflection losses. Assuming that the absorption and power diffracted into any order other than the +1 order is negligible, then the DE can be obtained using the spectral transmittance, $T(\lambda)$ with:

$$DE(\lambda) = 1 - T(\lambda). \tag{4.20}$$

The spectral transmittance for each hologram at different humidity levels is shown in Figure 17. Each curve represents a single hologram that is exposed independently and post processed in a group of 3 holograms. The plots show significant variation in the diffraction efficiency, even though the holograms were recorded using the same construction angles. Reduced diffraction efficiency is observed as shallower dips in the spectral transmittance. Additionally, many of the plots show variation along the horizontal axis.

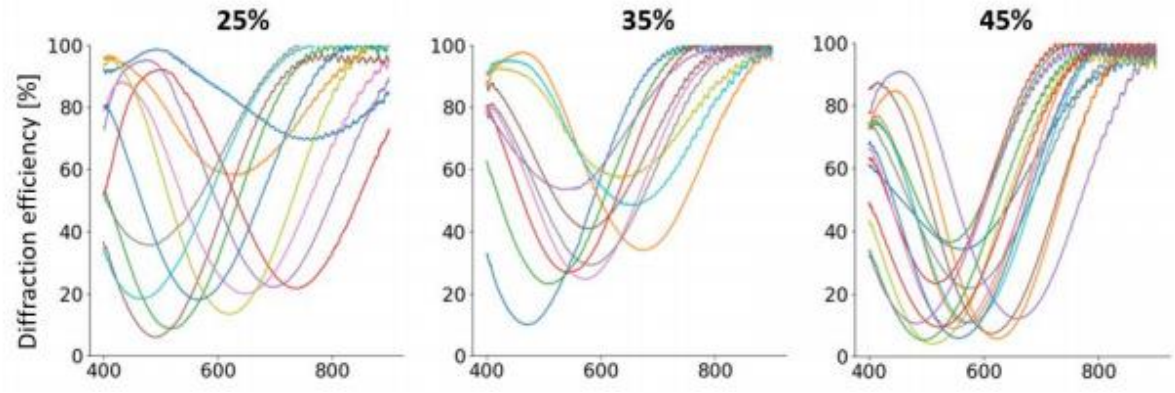

a) b) c)

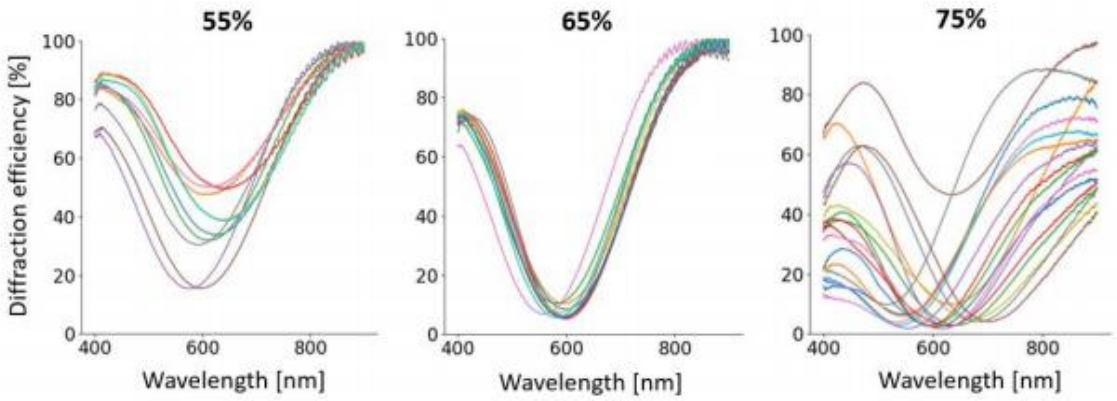

d) e) f)

Figure 17: Spectral transmittance for holograms formed in DCG dried at a) 25%, b) 35%, c) 45%, d) 55%, e) 65%, and f) 65%. Holograms are reconstructed with a broadband halogen lamp at normal incidence.

The results for each set of holograms are summarized in Figure 18. The standard deviation of the Bragg-matched wavelength for normally incident light and the standard deviation of the maximum diffraction efficiency as a function of humidity during the drying process are plotted. The Bragg wavelength is estimated as the wavelength that has the highest diffraction efficiency for each set. Figure 18 shows that the variation in the Bragg wavelength is at a maximum when using a drying humidity of 25%, which corresponds to a standard deviation of +/- 100 nm. The variation in the Bragg wavelength is at a minimum when the drying humidity used is 65%, which corresponds to a standard deviation of +/- 15 nm. Increasing the drying humidity above 65% results in an increase in the variation of the Bragg wavelength. Likewise, the variation in the maximum DE decreases from +/- 19% to +/- 2% when increasing the drying humidity from 25% to 65%. The variation in the maximum DE increases when drying humidity above 65%. A substrate with three holograms recorded on the film, dried at 65% humidity, is shown in Figure 19.

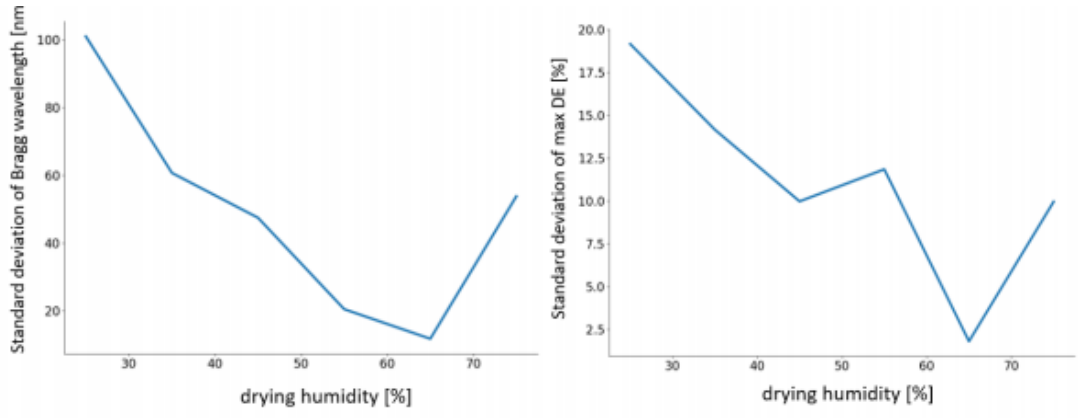

a) b)

Figure 18: Standard deviation in a) Bragg wavelength and in b) maximum DE attained at the Bragg wavelength for normally incident light with respect to drying humidity.

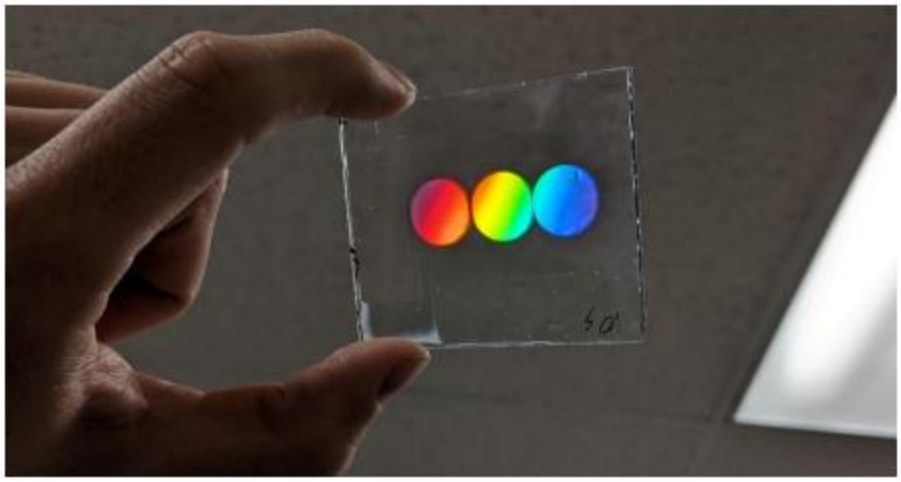

Figure 19: Three holographic gratings recorded in DCG dried at 65% humidity.

This section evaluates the effects of drying humidity during the drying process on the repeatability of the diffraction efficiency of transmission holograms recorded in DCG. A wavelength shift corresponding to variation along the horizontal axis can be explained by the film undergoing an inconsistent film swelling, which changes the Bragg condition. The inconsistent swelling is a reason why making holograms with DCG is not very repeatable. Figure

18 shows that drying the film in a controlled 65% humidity environment minimizes this variation. When the drying humidity is increased from 25% to 65%, the variation in the Bragg wavelength for normally incident light decreased from +/- 100 nm to +/- 15 nm, and the variation in the maximum diffraction efficiency decreased from +/- 19% to +/- 2%. Additionally, the variation in the Bragg wavelength and the variation in the maximum diffraction efficiency increases for drying humidity above 65%. To further investigate this issue, increasing the resolution of the drying humidity around 65% would be the next step. Currently, the makeshift dry box limits this possibility and would have to be upgraded to complete this step.

4.7: HOE Size Limitations

Another potential limitation of an agrivoltaic system is the ability to create large-scale holographic gratings. Two potential approaches to addressing this problem are monolithic and mosaiced HOEs [22]. For example, two large monolith Volume Phase Holographic Gratings (VPHGs) produced for an astronomy application at Centre Spatial de Liege (CSL) are 380 mm in diameter, as shown in Figure 20. However, large optics are needed for these recordings, meaning a higher cost and greater difficulty with stabilization.

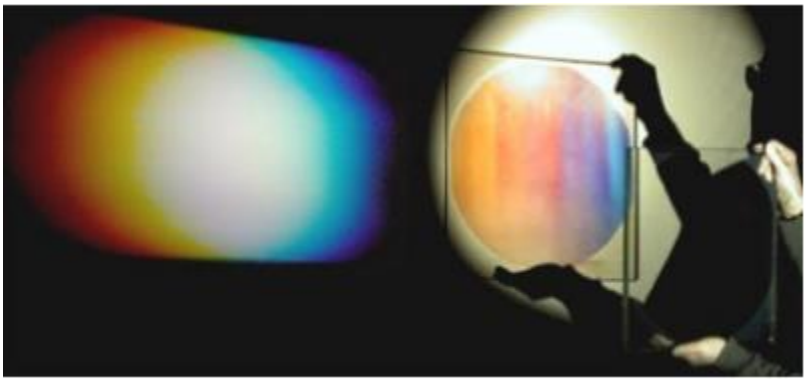

Figure 20: 380 mm diameter monolithic VPHG produced by CSL [22].

To avoid using larger optics, CSL also utilized a mosaic technique in which several gratings are recorded and processed independently, and then assembled [22]. This technique comes with unique challenges because each sub-element must diffract at the same angle and with the same efficiency, meaning the gelatin layer thickness and index modulation must be perfectly tuned. This task can be difficult with a material like DCG that can be relatively inconsistent. CSL has produced mosaiced VPHGs consisting of four elements for a total size of 240X340 mm, shown in Figure 21.

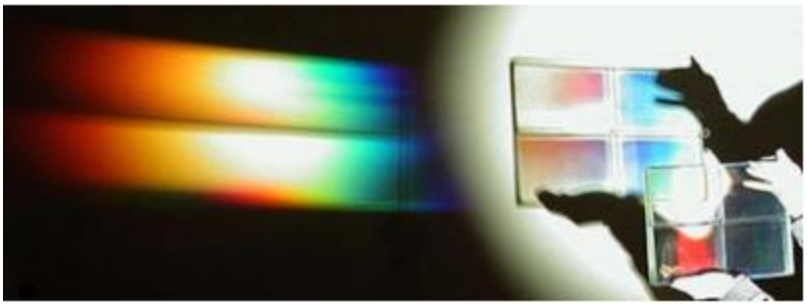

Figure 21: 240X340 mm mosaiced VPHG produced by CSL [22].

An additional method of mass producing volume HOES includes a one-beam recording scheme to copy a master volume holographic optical element in a step-and-repeat process and was demonstrated by Bruder et al. [26]. In this process Bayfol HX film is laminated to a master stack before being exposed by a scanning laser line. Holographic replication reduces the complexity of the optical setup as only one beam is needed. The master HOE creates an object beam that interferes with the illumination beam on copy film that is laminated to the master HOE. The copy film that has the copied volume HOE is then delaminated and re-masked with a new cover foil [26].

The most viable approach for mass manufacturing volumetric transmission holograms was demonstrated by Prism Solar Technologies. The patent describes a film roller system that

utilizes a holographic master plate opposing a pneumatic absorber that allows for strips of the recording film to be illuminated and then advance to allow for the next section of the strip to be recorded. This technique allows for the mass production of repeatable strips of holograms. In addition, holograms recorded using this process are certified for 25-30 years of sunlight exposure without significant degradation [27][28]. This product is used in the only commercialized holographic solar concentrator PV system.

Chapter 5: Applications of Holography

5.1: Cascaded Holograms

This section compares three designs to emphasize the potential improvement of cascaded holograms. Cascaded HOEs are often used in photovoltaic designs that incorporate HOEs as the cascaded configuration leads to a more extensive set of hologram design parameters [21]. The cascaded configuration can allow for a larger spectral and angular bandwidth to be diffracted onto the solar cell allowing for an increase in the conversion of solar energy to electricity; however, this can also introduce cross-coupling losses. Cross-coupling results from overlapping hologram diffraction efficiencies which means that the diffraction angle of the first hologram matches the diffraction angle of the second hologram [21]. When this occurs, the diffracted spectral component does not reach the solar cell, leading to decreased energy conversion efficiency.

The following modeled diffraction efficiency plots are obtained by using the Approximate Coupled Wave Analysis model outlined in Section 4.2. Diffraction efficiency (DE) and diffraction angle are both multiple dimensional plots that depend on incident zenith and azimuthal angles and the wavelength of the incident light. In the out-of-plane direction, the peak wavelength is much less dependent on the incident angle and is much less sensitive in the x-z plane [21]. The acceptance angle is the angular range over which the optical efficiency is above a specified threshold [21]. For a fixed PV panel tilted at the latitude angle facing due south, the acceptance angle should be approximately +/- 23° to allow for seasonal variations in the sun's declination angle [21]. This means that the DE should remain high over an incident angle range of +/- 23° over the wavelength range to which the PV cell is sensitive. For a silicon solar cell, this range is from 400-1100 nm. A two-dimensional DE plot showing the DE as a function of

wavelength and in-plane (y-z plane) angle is a helpful tool to verify the effectiveness of a holographic solar concentrator. Figure 22 a) shows a design that only uses one holographic grating to diffract light towards a PV cell. Figure 22 b) shows the 2-D DE plot for the holographic grating with construction parameters outlined in Table 2. Contours where the diffraction efficiency is equal to 30% are shown.

Table 2: Construction parameters that correspond to the 2-D DE plot shown in Figure 22.

θ_{con}	22°
θ_{ref}	70°
λ_{con}	532 nm
Grating Thickness	3 μm
Effective Index Modulation	0.09

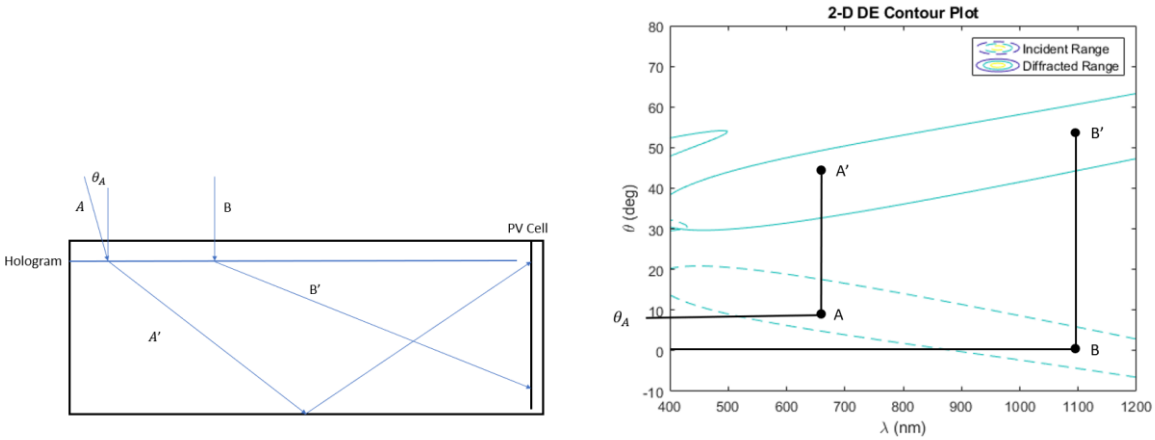

a) b)

Figure 22: a) Illustration of a holographic design that diffracts light toward a PV cell using a single holographic grating; b) 2-D DE Contour Plot at 30% efficiency with the construction parameters outlined in Table 2. The width to height ratio of the design is chosen to be 1.8 to allow all light that undergoes total internal reflection to be incident on the PV cell.

Figure 22 shows that a single hologram can efficiently collect over an angular range of 0-10 degrees at a specific wavelength. Incident light within this 0-10 degree range (dashed line) diffracts to a larger angle shown in the solid line (A → A', B → B'). B corresponds to an incident ray with normal incidence and is diffracted at an angle of 50 degrees. Diffracted rays can reach the PV cell by direct diffraction when diffracted at a large enough angle, such as shown by Ray B. Additionally, rays that do not diffract at a large enough angle can reach the PV cell after multiple internal reflections, such as shown by Ray A. The diffraction process is reciprocal, meaning that the incident range and the diffracted range are interchangeable. Using a single holographic optical element does not provide the desired acceptance angle range of +/- 23°. Therefore, cascaded holographic gratings are often used for non-tracking solar applications.

For a holographic planar concentrator (HPC) with a fixed tilt angle equal to the latitude, two cascaded holograms can capture most of the incident solar energy throughout the year [21]. Figure 23 shows a similar design that incorporates a cascaded pair of holographic gratings to diffract light toward a PV cell and the 2-D DE contour plot for the cascaded holographic grating pair. The construction parameters for both holograms are shown in Table 3.

Table 3: Construction parameters that correspond to the 2-D DE plot shown in Figure 23.

	H1	H2
θ_{con}	22°	9°
θ_{ref}	70°	50°
λ_{con}	532 nm	532 nm
Grating Thickness	$3\mu m$	$3\ \mu m$
Effective Index Modulation	0.09	0.09

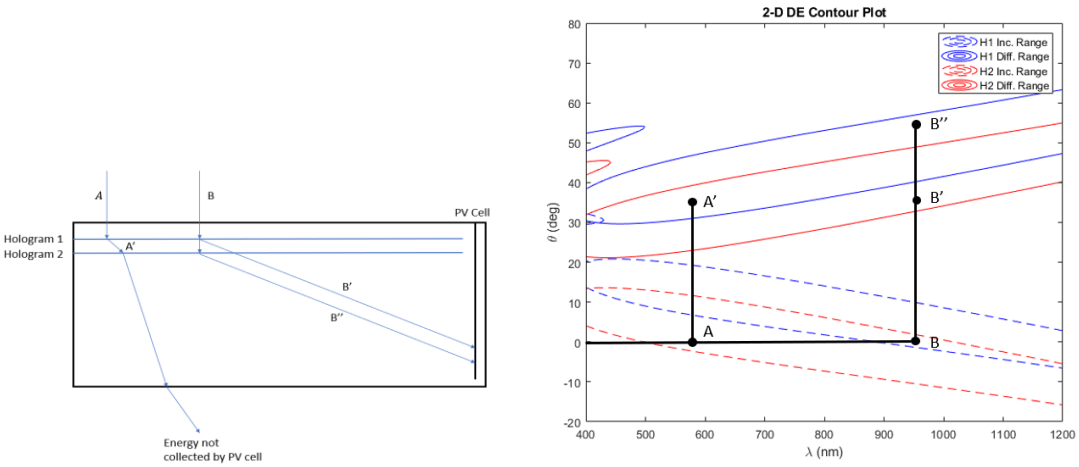

a) b)

Figure 23: a) Illustration of a holographic design that diffracts light toward a PV cell using a cascaded pair of holographic gratings; b) 2-D DE Contour Plot at 30% efficiency with the construction parameters outlined in Table 3. As this design is meant to be compared to the design in Figure 22, the width to height ratio is again selected to be 1.8 to allow for light that is totally internally reflected to be incident on the PV cell.

As discussed in an earlier section, the cascading of holograms can lead to cross-coupling losses, which leads to a reduction in output power. The overlap in the incident range does not lead to cross-coupling losses, as shown with Ray B. Ray B is within both the first and second hologram's incident angle range and thus will be partially diffracted by both holograms. However, the overlap in the diffraction range will lead to cross-coupling losses, as shown by Ray A. Ray A will be diffracted by the first hologram and then will be re-diffracted by the second hologram at an angle that will not undergo total internal reflection and will therefore not reach the PV cell area. This could be beneficial in an agrivoltaic application as this cross-coupled light could reach the crop area below.

The cascaded hologram design can be modified such that the diffraction ranges for both holograms do not overlap. For example, in Figure 24, two holographic gratings are designed to diffract light in different directions towards two different PV cells to reduce cross-coupling. The 2-D DE contour plot is also shown.

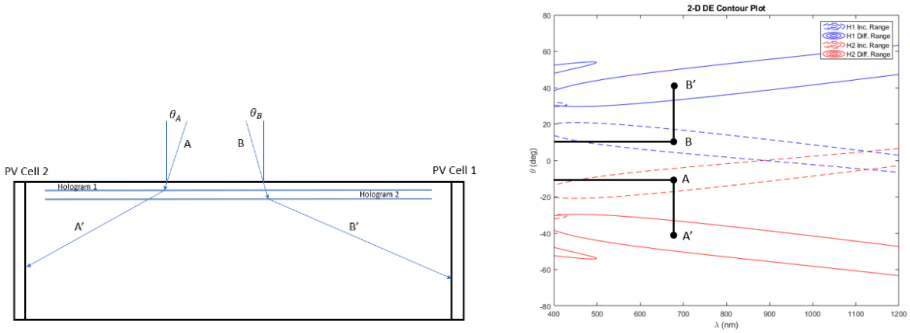

Figure 24: a) Illustration of a holographic design that uses two cascaded holograms. Hologram 1 diffracts light toward PV cell 2, and Hologram 2 diffracts light toward PV cell 1; b) 2-D DE Contour Plot at 30% efficiency. Using the same width to height ratio as the previous two designs of 1.8, using cascading holograms to diffract in opposing directions can nearly double the amount of light that is incident onto the PV cell area.

5.2: Example Systems that Combine HOEs and PV Cells

Various proposed photovoltaic module designs incorporate HOEs; however, only a select few have ever made it to commercial production. These designs differ in their application of holograms, from using reflection or transmission holograms to using single layer, cascaded, or multiplexed holograms. One common factor among the designs is the goal to increase the energy conversion efficiency of the system. One such proposed design is shown in Figure 25. This design utilizes a single holographic grating and one PV cell. The light is diffracted by the hologram and guided via total internal reflection onto the PV cell. However, due to the

hologram's inherent chromatic and angular selectivity, much of the energy is not diffracted by the grating and is unused.

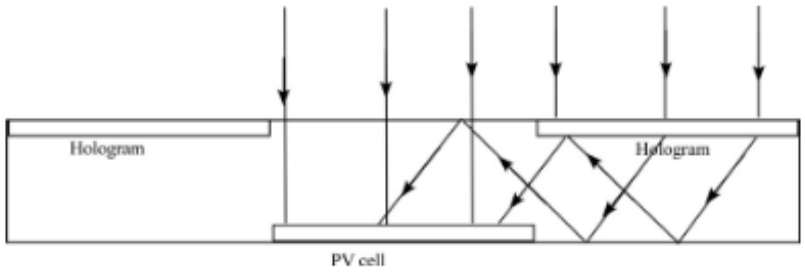

Figure 25: Design proposed by Zhang et al. [29].

For this reason, many systems combine various optical elements to collect a greater fraction of the incoming solar irradiation by effectively increasing the chromatic and angular bandwidth of the HOE. Consequently, increased efficiency often comes at the price of increased design complexity and cost. The following designs in Figures 26 and 27 demonstrate a more complicated approach incorporating cascaded holograms.

The cascaded HOE design in Figure 26 is one approach to addressing the limited chromatic selectivity of holograms. The first holographic grating in the cascaded pair diffracts longer wavelengths toward a PV cell with spectral sensitivity to longer wavelengths, whereas the second holographic grating diffracts shorter wavelengths to a PV cell with spectral sensitivity at shorter wavelengths. The opposing direction of diffraction for both holograms eliminates the crosstalk between diffracted beams. This creates a photovoltaic system that captures more of the incoming spectrum from the sun; however, angular selectivity is still problematic, and tracking would likely be required.

The cascaded HOE design in Figure 27 involves increasing the range of incident angles diffracted onto the PV cell. Gratings A and A' are conjugates that diffract at angles close to normal incidence but opposite to one another. Likewise, for gratings B and B', the conjugate gratings are designed for larger angles in reference to normal incidence. The opposing direction of diffraction for both holograms decreases the cross-coupling between diffracted beams. Although this design addresses the limited angular bandwidth and reduces the need for a tracking system, the design does little to address the multispectral characteristic of the sun.

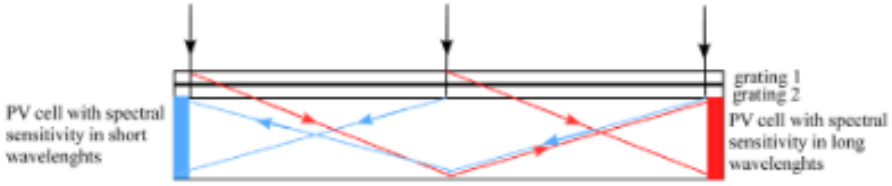

Figure 26: Design proposed by Kostuk et al. Two cascaded holographic gratings are used to increase the range of wavelengths operable for the system while decreasing crosstalk [30].

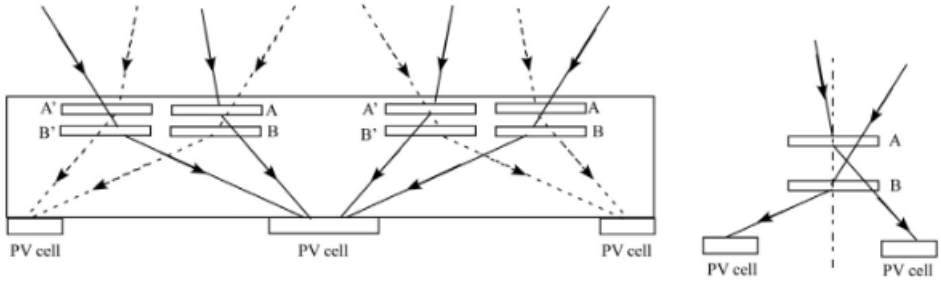

Figure 27: Design proposed by Castro et al. Two cascaded gratings are used to increase the range of incident angles operable for the system while decreasing cross coupling losses [31].

The design in Figure 28 adopts another widely considered approach that uses bifacial silicon cells. Bifacial cells collect light that is incident on both the front and back face of the cell. This design uses a pair of holographic gratings in addition to total internal reflection to increase

the amount of light that is incident on both faces of the cell. Grating 1 diffracts radiation to the cell on the left and grating 2 diffracts radiation to the cell on the right. To address dispersion due to the grating, the longer wavelengths that are diffracted at a larger angle are collected on the backside of the bifacial cell, and shorter wavelengths that diffract at a smaller angle are collected on the front side of the cell. Bifacial PV systems also collect albedo illumination from the ground or other nearby surfaces. In order to operate at ideal efficiency conditions, this system would also require solar tracking.

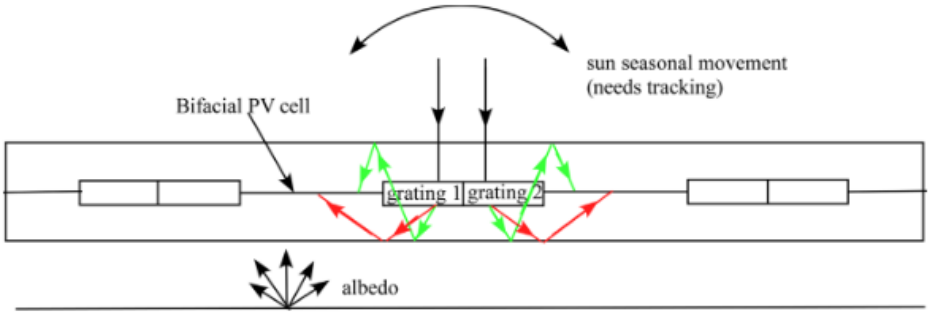

Figure 28: Design proposed by Castillo et al., which uses two holographic gratings combined with a bifacial cell [32].

Holographic lenses have also been used for photovoltaic system applications. Chromatic dispersion causes the lens to focus light of different wavelengths to different positions. This characteristic can be utilized to focus different wavelengths onto different cells that are more sensitive to that wavelength. For example, one proposed design that uses holographic transmission lenses is shown in Figure 29. Each holographic lens is combined with two different PV cells. The holographic lens focuses smaller wavelengths to the type 1 PV cell, which can more efficiently convert energies at these wavelengths to electricity. Likewise, the longer wavelengths focus on the type 2 PV cell, which can more efficiently convert energies at these

wavelengths to electricity. However, as with most proposed designs, solar tracking is essential to maintain ideal conditions for increased energy conversion efficiency.

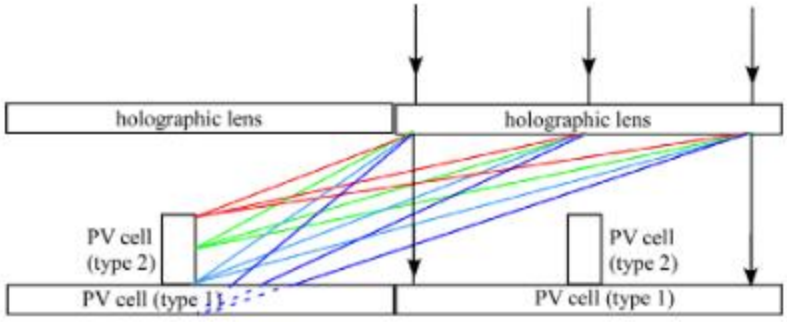

Figure 29: Design proposed by Zhang et al. using holographic lenses to focus different wavelengths of the solar spectrum onto PV cells that are more efficient at converting solar energy to electricity at those wavelengths [33].

In summary, over recent years, there has been a growing interest in photovoltaic modules as a source of clean, renewable energy as there is a steadily growing need for a rapid transition to a sustainable and low carbon future. Adding HOEs to increase the efficiency of these photovoltaic modules has attracted growing attention, but this technique comes with its own difficulties and limitations. Most importantly, volume HOEs have a limited angular and spectral bandwidth in which diffraction is efficient. Various configurations of photovoltaic modules implementing HOEs have been proposed to overcome these limitations; however, only one design by Prism Solar Technologies has been commercialized. Nonetheless, volume holograms can manipulate an illumination spectrum in ways that are advantageous. The potential goes beyond that of solar panels and can also be applied to satisfy thermal, medical, and agricultural needs. Chapter 7 describes an agrivoltaic design that splits the incoming solar spectrum to support both photovoltaic energy generation and agricultural crop production.

Chapter 6: System Analysis

6.1: System Model

Power generated by a PV cell for light directly illuminating the cell area is given by:

$$P_{PV1,PV2}(t, d_n) = F_{o-e} A_{PV} \cos[\theta_i(t, d_n)]\, T[\theta_i(t, d_n)] \times \int SR(\lambda) E(\lambda) d\lambda, \quad (6.1)$$

where $F_{o-e} = FF * V_{oc}$ is assumed to be a constant, $FF = \frac{P_{max}}{I_{sc} * V_{oc}}$ is the fill factor, A_{PV} is the area of the PV cell, and $T(\theta_i)$ is the transmittance coefficient of unpolarized light given by:

$$T(\theta_i) = 1 - 0.5[R_p(\theta_i) + R_s(\theta_i)]. \quad (6.2)$$

$R_p(\theta_i)$ and $R_s(\theta_i)$ are the intensity reflection coefficients for *s*- and *p*- polarized light and are given by:

$$R_s(\theta_i) = \left[\frac{n_1 \cos(\theta_i) - n_2 \cos(\theta_t)}{n_1 \cos(\theta_i) + \cos(\theta_t)}\right]^2, \quad (6.3)$$

$$R_p(\theta_i) = \left[\frac{n_1 \cos(\theta_t) - n_2 \cos(\theta_i)}{n_1 \cos(\theta_t) + \cos(\theta_i)}\right]^2, \quad (6.4)$$

respectively. θ_t is the transmitted beam angle using Snell's Law. E is the direct normal solar irradiance incident onto a surface perpendicular to the sun. This value is assumed to be constant, corresponding to an air mass of 1.5 (AM1.5), as shown in Figure 1. Power generated by solar illumination diffracted by the cascaded hologram pair onto either PV cell is given by:

$$P_{H1,H2}(t, d_n) = F_{o-e} A_H \cos[\theta_i(t, d_n)]\, T[\theta_i(t, d_n)] \times \int SR(\lambda) DE[\lambda, \theta'(t, d_n), \phi'(t, d_n)] E_{AM1.5}(\lambda) d\lambda. \quad (6.5)$$

$\theta'(t, d_n)$ and $\phi'(t, d_n)$ are the incident zenith and azimuthal angles in the grating medium, A_H is the area of the hologram, and DE is the diffraction efficiency of a hologram.

The energy corresponding to the PAR region is also simulated using a similar method. The power going to the crop area corresponds to the incident solar irradiance diffracted but not incident onto the solar panels and the incident solar irradiance transmitted through both holograms. Only radiation from 400-700 nm is considered for the results.

6.2: Solar Illumination Model

The solar declination angle δ is a function of the day of the year DoY, and is assumed to be constant over the duration of the day,

$$\delta \approx 23.45 * \sin\left(\frac{360}{365} * (DoY + 284)\right). \tag{6.6}$$

The elevation and azimuth angles are functions of the declination angle, latitude, and hour angle (HRA) and are given by:

$$\theta_{ele} = \text{asin}(sin(\delta) * sin(lat) + cos(\delta) * cos(lat) * cos(HRA)), \tag{6.7}$$

$$\varphi_{azi} = \text{acos}(sin(\delta) * sin(lat) - cos(\delta) * sin(lat) * cos(HRA)). \tag{6.8}$$

The hour angle is a conversion from the local solar time into the number of degrees that the sun moves across the sky. At any latitude, when the sun is at the highest position in the sky (solar noon) the HRA = 0. Since the Earth moves at 15° per hour, each hour away from solar noon corresponds to an angular motion of the sun of 15° in the sky. The zenith angle is given by:

$$\theta_{zen} = 90 - \theta_{ele}. \tag{6.9}$$

6.3: Annual Energy Yield Calculation

For a given day number, DoY, the daily energy yield for a two PV panel system that captures light from a pair of cascaded holograms is given by:

$$E_{day,\ PV}(DoY) = \int (P_{pv1} + P_{pv2} + P_{H1} + P_{H2})dt, \tag{6.10}$$

where P_{pv1}, P_{pv2}, P_{H1} and P_{H2} are defined in Section 5.1.2. Because the cascaded holographic gratings diffract light in different directions, two PV cells are used in modelled design to collect light that is diffracted by either hologram. The annual energy yield of the system is calculated by summing the daily energy yield over 365 days of the year:

$$E_{annual} = \sum E_{day}(DoY). \tag{6.11}$$

The daily and annual energy incident onto the crop area is calculated in the same way.

Chapter 7: Holographic Agrivoltaic System Design

7.1: Design Description

For a non-tracking HPC system, the fringe direction aligns with the motion of the sun to maximize energy collection because diffraction efficiency is less sensitive to the out-of-plane direction, as shown in Figure 29 a) [21]. The agrivoltaic design that is modeled is shown in Figure 29 b) and c).

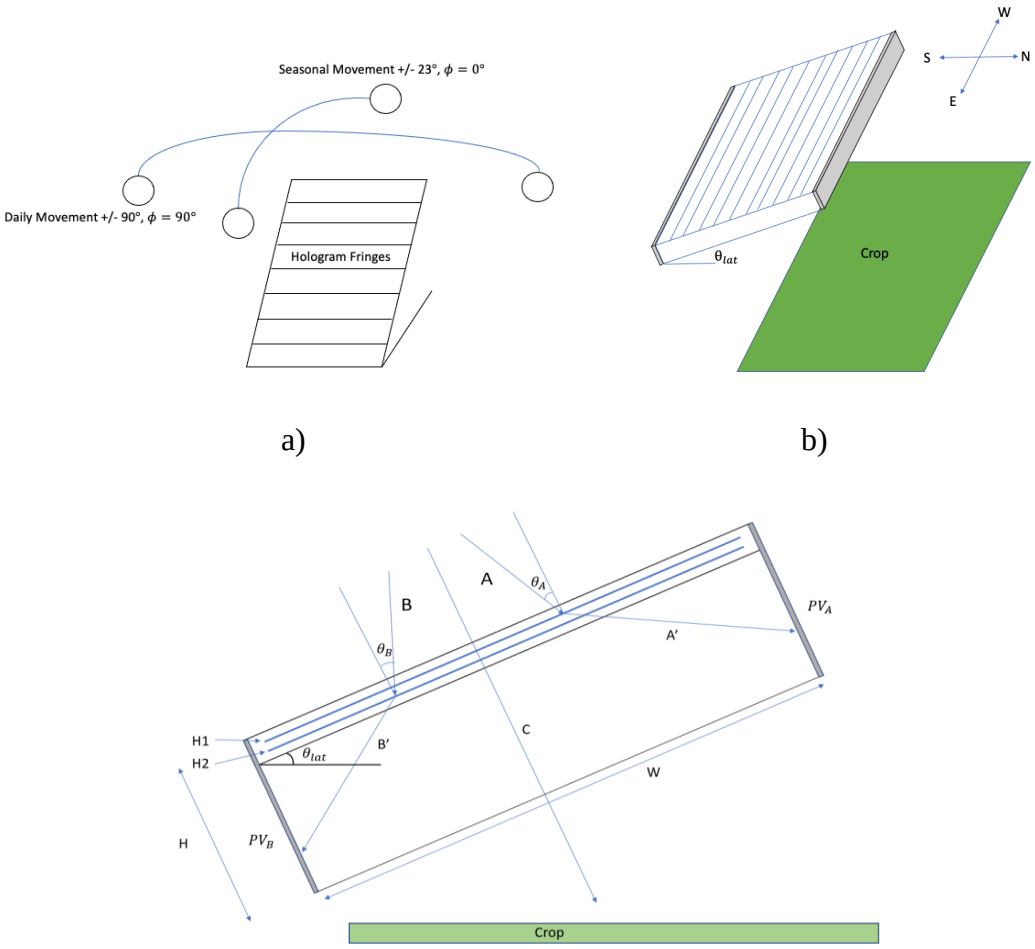

Figure 30: a) Optimal fringe orientation for non-tracking holographic planar concentrator b) modeled agrivoltaic greenhouse design, and c) side view of agrivoltaic design.

The design incorporates a cascaded holographic grating pair and a PV cell on both the northern and southern sides of the module. The cascaded holographic pair are at a fixed tilt angle equal to the latitude. The construction parameters for each hologram are shown in Table 4. Assuming the refractive index of the glass substrate is 1.5, the width to height ratio of the module is selected to be 1.8 to ensure that all light that undergoes total internal reflection is collected by the PV cell.

Table 4: Construction parameters that correspond to the 2-D DE plot in Figure 30 for the modeled agrivoltaic greenhouse design.

	H1	H2
θ_{con}	22°	-22°
θ_{ref}	70°	-70°
λ_{con}	532 nm	532 nm
Grating Thickness	$3\mu m$	$3\ \mu m$
Effective Index Modulation	0.09	0.09

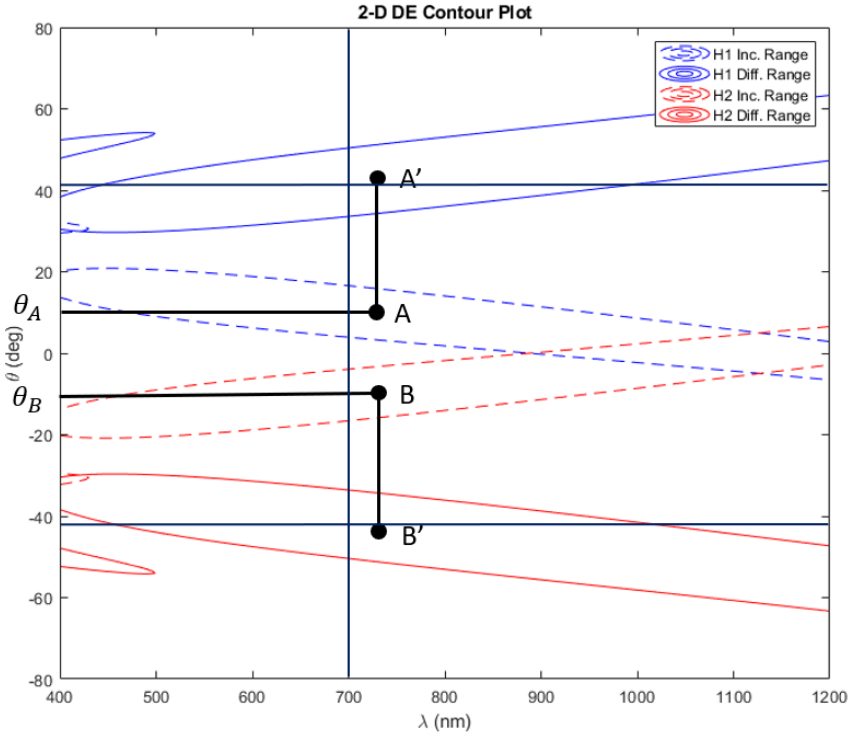

Figure 31: 2D DE plot for the proposed agrivoltaic design.

Hologram 1 is designed such that the solar illumination during the winter months is efficiently diffracted toward the northern PV cell, and hologram 2 is designed such that solar illumination in the summer months is efficiently diffracted toward the southern PV cell. Ray A represents direct illumination from the sun during the winter months at an incident angle θ_A with respect to the surface normal. This ray is diffracted at a larger angle such that it can be collected by the northern PV cell. Ray B illustrates the analogous process for the summer months. Ray C, as shown in Figure 30 c), represents solar illumination during the spring and fall months when the solar noon elevation does not reach the summer month maximum nor the winter month minimum. During these months, the energy produced by the PV cell is at a minimum. The northern PV cell also collects a portion of the non-diffracted solar illumination during the winter months. In contrast, the southern PV cell collects a portion of the non-diffracted solar illumination during the summer months.

To address the overlapping spectral range of the crop and the silicon PV cell, the holograms are constructed such that most of the light below 700 nm does not undergo total internal reflection and is transmitted to the crop area below. Above 700 nm, corresponding to light that the crop is not sensitive to, the holograms are designed such that most the light is diffracted at an angle greater than the critical angle to ensure total internal reflection allowing the ray to be collected onto either PV cell.

7.2: Simulation Results

The power generation rate throughout the year is evaluated at 5-min intervals. The daily and annual energy yields are calculated by integration as described in Chapter 6. The results are simulated for a latitude of 32 degrees The daily energy yields for both the PV cell and the greenhouse design crop area are shown in Figures 32 a) and b). The annual energy incident onto

the crop area corresponding to the PAR region for the modeled agrivoltaic system is 708.762 kWh/m^2. The annual energy yield of the PV cell is 264.836 kWh/m^2. The maximum solar radiation available to a fixed tilt array at the latitude angle and a dual axis tracking array in Tucson, Arizona is approximately 2370 $kWh/m^2/yr$ and 3285 $kWh/m^2/yr$, respectively.

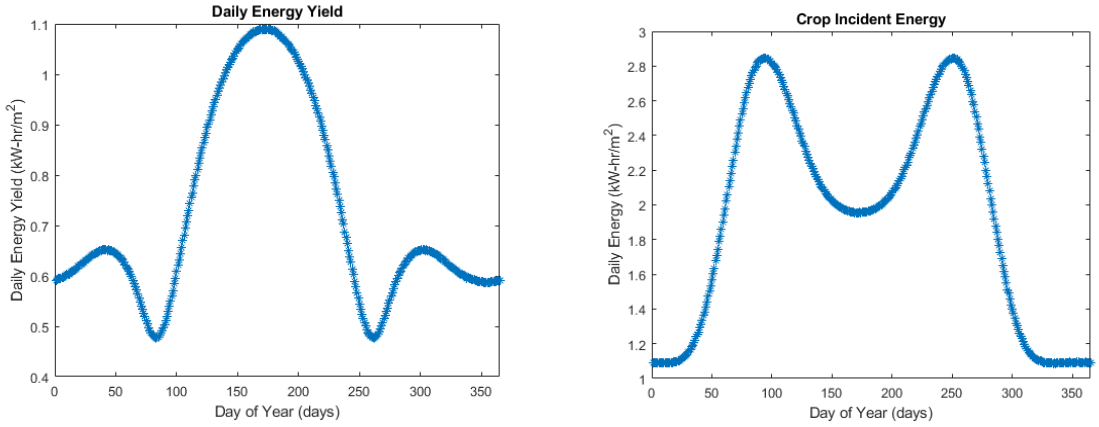

a) b)

Figure 32 a) The daily energy yield simulated throughout a year for the PV module and b) the daily incident PAR energy simulated throughout a year for the crop area.

There are dips in the PV daily energy yield near days 80 and 260 because the conditions are not met for the hologram to efficiently diffract the incoming solar illumination. The majority of the illumination incident onto the cascaded hologram pair is transmitted through the pair onto the crop area below the PV module as can be seen in an increase in the crop incident energy during these days. Conversely, the direct solar illumination incident onto the hologram pair around solar noon near days 35, 180, and 310 satisfies the conditions for the holograms to diffract efficiently. Thus, the daily energy yield for the PV cell increases during these days. Figure 33 shows the PAR energy that is incident onto the crop area for three different days.

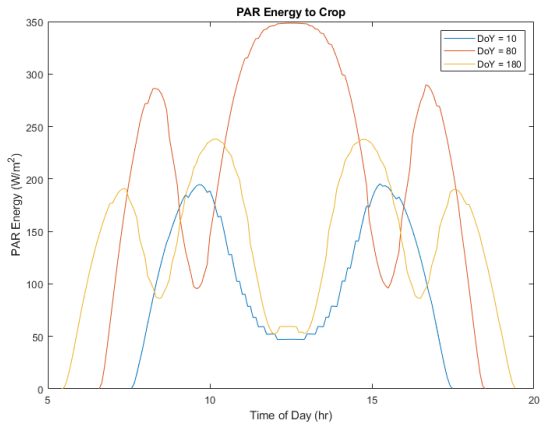

Figure 33: PAR energy incident onto the crop area for three days of the year.

Figure 33 shows that the PAR energy incident on the crop area significantly decreases on days 10 (blue curve) and 180 (yellow curve) around noon; however, it only shows minor dips on day 80 (orange curve). The magnitude and duration of the dips vary throughout the year. The winter, represented by the blue line, shows a relatively shallower but more prolonged dip, lasting approximately 5 hours. However, for the summer, represented by the yellow line, the dip is deeper but only lasts approximately 2 hours around noon. Additionally, as the sun is rising and setting, there are additionally dips showing that the conditions for efficient diffraction by the second hologram are met during these times. Around noon in spring, shown by the orange line, the incoming solar irradiation does not efficiently diffract, and therefore, there is no solar noon dip. However, as the sun is rising and setting, some of the incoming solar irradiation is diffracted and resulting in small dips in the energy incident onto the crop area around hours 9 and 15.

The photovoltaic performance of the agrivoltaic design is compared to six different PV systems: fixed-tilt PV cell and holographic planar concentrator (HPC), horizontal one-axis tracking PV cell and HPC, and polar one-axis tracking PV cell and HPC [18]. An HPC is a system in which HOEs diffract usable frequencies of the incident solar illumination towards

strips of solar cells. The efficiencies of the PV cells are assumed to be constant over the operating irradiance and temperature range. Horizontal one-axis tracking refers to the tracker rotating around a horizontal N-S tracker. Polar tracking refers to the tracker rotating around an axis inclined at the latitude angle in the N-S direction. The annual energy yields of each system are shown in Table 5.

Table 5: Annual energy yield comparison between the modeled greenhouse design and six different PV systems as outlined in [21].

System	**Fixed Tilt**		**Horizontal 1-axis**		**Polar 1-axis**		**Fixed Agrivoltaics**
Type	**PV**	**HPC**	**PV**	**HPC**	**PV**	**HPC**	**HPC**
Annual Energy Yield ($kW-hr/m^2$)	401.5	310.7	505.9	426	530.7	446.9	264.836

The results show that the annual energy yield for the modeled agrivoltaic greenhouse design will provide 66% of the energy produced by a conventional non-tracking fully populated PV cell, 85% of the energy produced by a similar non-tracking HPC system, and only 50% of the energy produced by a polar one-axis fully populated PV cell [21]. Although the energy yield for this agrivoltaic system is lower than the other designs, this design allows for much of the solar radiation to be incident onto the crop area below.

As currently designed, the system is optimized for crops that have a growing season in the spring or the fall when diffraction by the cascaded holographic gratings is less efficient. Additionally, plants could benefit from shading in these months as a fraction of the light is still diffracted toward the PV cells. This potentially beneficial shading is evident in the summer months as well and could result in a prolonged growing season as crops could be less susceptible

to over exposure. The design parameters of the hologram pair could be varied to optimize for a variety of different crops that need different conditions to thrive, such as spectral radiation, growing season, and shade tolerance. A deeper consideration and analysis of various crop is required to better understand if an agrivoltaic system such as the one proposed is viable.

Chapter 8: Conclusion

Agrivoltaics has received growing attention in recent years as a potential solution to issues brought on by climate change and population growth. Agrivoltaics could be beneficial to both food production and energy production as the colocation of photovoltaics and agriculture could result in reduced evaporative losses, increased CO_2 uptake, and a cooler local climate. Holographic optical elements are one technology that could be utilized to split the solar spectrum into the PAR spectral bandwidth optimal for plant growth, and the spectral bandwidth photovoltaic cells are most sensitive to due to their angular and spectral selectivity characteristics. Additionally, holographic optical elements can be cascaded to increase the angular and spectral bandwidth of the diffracted region.

One photosensitive material that could prove optimal for an agrivoltaic application is dichromated gelatin. DCG is inexpensive to produce, allows for a large refractive index modulation, allows control over many design parameters, has excellent resilience to temperature fluctuation, and is stable for years if sealed properly. However, DCG is challenging to work with, and it can be difficult to obtain consistent and repeatable results without a controlled environment. The drying process of the DCG film can contribute to inconsistent results. A drying humidity of 65% during the drying process has been shown to minimize the variation in both the Bragg wavelength and the maximum diffraction efficiency of holograms formed in DCG.

An agrivoltaic design that incorporates two cascaded linear holographic gratings is modeled and analyzed. Results show that the agrivoltaic design can provide 66% of the annual energy produced by a conventional non-tracking fully populated PV cell and 85% of the energy produced by a non-tracking HPC system. Although the agrivoltaic design provides a lower annual energy yield than other PV systems, much of the solar radiation is incident onto the plants

below. In the proposed design, the daily energy yield is optimized for the winter and summer months because, during these months, the holograms diffract more efficiently. This results in a dip for approximately 5 hours in the amount of energy reaching the crop area in the winter, whereas in the summer, the dip in energy reaching the crop area is approximately 2 hours. This design allows for the available PAR during sunrise and sunset to be incident on the plant when the available PAR is lower than the saturated PAR for the plants and diffracts a fraction of the available PAR to the PV cell around noon when the available PAR can exceed what the crop needs, reducing crop productivity. During the spring and fall, the daily energy yield is decreased compared to the winter and summer because the cascaded holograms do not efficiently diffract. This is due to the sun's position in the spring and fall. This lack of diffraction leads to increased incident energy onto the crop area, resulting in improved plant productivity. A more extensive investigation into various types of crops and solar illumination conditions that can support optimal plant productivity is the next step in determining if an agrivoltiac design such as the one proposed is viable for a specific application.

Works Cited

[1] United Nations, Department of Economic and Social Affairs, Population Division (2019). *World Population Prospects 2019, Volume II: Demographic Profiles* (ST/ESA/SER.A/427).

[2] U.A. Schneider, P. Havlík, E. Schmid, H. Valin, A. Mosnier, M. Obsteiner, H. Böttcher, R. Skalsky, J. Balkovič, T. Sauer, S. Fritz, "Impacts of population growth, economic development, technical change on global food production and consumption," Agricultural Systems 104(2), 204-215 (2011).

[3] IEA (2020), *World Energy Outlook 2020*, IEA, Paris.

[4] H. Ritchie, "Energy mix," Energy - Our World in Data.

[5] R. Quadrelli, S. Peterson, "The energy-climate challenges: Recent trends in CO_2 emissions from fuel combustion," Energy Policy 35(11), 5938-5952 (2007).

[6] BW. Brook, A. Alonso, D.A. Meneley, J. Misak, T. Blees, J.B. van Erp, "Why nuclear energy is sustainable and has to be part of the energy mix," Sustainable Materials and Technologies 1-2, 8-16, (2014).

[7] R.K. Kostuk, "Introduction Lecture," Photovoltaic Solar Energy Systems (2019).

[8] MA Green, "Photovoltaic technology and vision for the future," Progress in Energy 1(1) (2019).

[9] R.K. Kostuk, "Photovoltaic Cells Introduction," Photovoltaic Solar Energy Systems (2019).

[10] C. Honsberg, S. Bowden, "P-n Junctions," PVCDROM.

[11] C. Honsberg, S. Bowden, “IV Curve,” PVCDROM.

[12] C. Honsberg, S. Bowden, "Spectral Response," PVCDROM.

[13] H. Imran, H. Riaz, N.Z. Butt, "Optimization of Single-Axis Tracking of Photovoltaic Modules for Agrivoltaic Systems," 2020 47th IEEE Photovoltaic Specialists Conference (PVSC), 1353-1356 (2020).

[14] G.A. Barron-Gafford, M.A. Pavao-Zuckerman, R.L Minor, L.F. Sutter, I. Barnett-Moreno, D.T. Blackett, M. Thompson, K. Dimond, A.K. Gerlak, G.P. Nabhan, J.E Macknick, "Agrivoltaics provide mutual benefit across the food-energy-water nexus in drylands," Nature Sustainability 2, 848-855 (2019).

[15] M. Trommsdorff, J. Kang, C. Reise, S. Schindele, G. Bopp, A. Ehmann, A. Weselek, P. Hogy, T. Obergfell, "Combining food and energy production: Design of an agrivoltaic system applied in arable and vegetable farming in Germany," Renewable and Sustainable Energy Reviews 140 (2021).

[16] A. Weselek, A. Ehmann, S. Zikeli, I. Lewandowski, S. Schindele, P. Hogy, "Agrophotovoltaic systems: applications, challenges and opportunities. A review," Agron. Sustain. Dev. 39, 35 (2019).

[17] 3M^{TM} Dichroic Glass Finishes DF-PA-Blaze, (3M Center, St. Paul, MN, Building 220-12E-04).

[18] G. Mittelman, H. Vitoshkin, B. Lew, H. Mamane, A. Kribus, "Innovative Solar Spectral Beam Splitting Concepts: Cogeneration and Photochemistry," 35th European Photovoltaic Solar Energy Conference and Exhibition.

[19] R.K. Kostuk, *Holography: Principles and Applications* (CRC Press, 2019).

[20] M.V. Collados, D. Chemisana, J. Atencia, "Holographic solar energy systems: The role of optical elements," Renewable and Sustainable Energy Review 59, 130-140, (2016).

[21] D. Zhang, J.M Castro, R.K. Kostuk, "One-axis tracking holographic planar concentrator system," J of Photonics for Energy 1(1), 015505 (2011).

[22] P.A. Blanche, C. Jamar, P. Gally, "Volume phase holographic gratings: Large size and high diffraction efficiency," Optical Engineering, 43(11) (2004).

[23] BD. Chrysler, E.J. Salay, R.K. Kostuk, "Improving the repeatability of the spectral bandwidth and diffraction efficiency of holograms formed in dichromated gelatin," Proc. SPIE 11367, Photosensitive Materials and their Applications, 1136718 (2020).

[24] Bayfol® HX200, (Covestro AG, LEverkusen, Germany).

[25] Rain-X® Original Glass Water Repellent, (ITW Global Brands, Houston, TX).

[26] F.K. Bruder, et al. "Mass production of volume holographic optical elements (vHOEs) using Bayfol (R) HX photopolymer film in a roll-to-roll copy process." Practical Holography XXXI: Materials and Applications. Vol. 10127. International Society for Optics and Photonics, (2017).

[27] E.D. Aspnes, et al. “Volume hologram replicator for transmission type gratings.” *US Patent* No. 8614842B2 (2013).

[28] J.T. Sheridan, et al. “Roadmap on holography.” *J. Opt.* 22 123002 (2020)

[29] R.K. Kostuk, G. Rosenberg, "Analysis and design of holographic solar concentrators," Proc. SPIE 7043, High and Low Concentration for Solar Electric Applications III, 704301 (2008).

[30] J.M. Castro, D. Zhang, B. Myer, R.K. Kostuk, "Energy collection efficiency of holographic planar solar concentrator," Appl. Opt. 49, 858-870 (2010).

[31] J.E. Castillo, J.M. Russo, R.K. Kostuk, G.A. Rosenberg, "Thermal effects of the extended holographic regions for holographic planar concentrator," J. of Photonics for Energy 1(1), 015504 (2011).

[32] D. Zhang, M. Gordon, J.M. Russo, S. Vorndron, R.K. Kostuk, "Spectrum-Splitting photovoltaic system using transmission holographic lenses," J. of Photonics for Energy 3(1), 034597 (2013).